

Measurement of neutral mesons in $p + p$ collisions at $\sqrt{s} = 200$ GeV and scaling properties of hadron production

A. Adare,¹¹ S. Afanasiev,²⁵ C. Aidala,^{12,36} N. N. Ajitanand,⁵³ Y. Akiba,^{47,48} H. Al-Bataineh,⁴² J. Alexander,⁵³ K. Aoki,^{30,47} L. Aphecetche,⁵⁵ R. Armendariz,⁴² S. H. Aronson,⁶ J. Asai,^{47,48} E. T. Atomssa,³¹ R. Averbeck,⁵⁴ T. C. Awes,⁴³ B. Azmoun,⁶ V. Babintsev,²¹ M. Bai,⁵ G. Baksay,¹⁷ L. Baksay,¹⁷ A. Baldissieri,¹⁴ K. N. Barish,⁷ P. D. Barnes,³³ B. Bassalleck,⁴¹ A. T. Basye,¹ S. Bathe,⁷ S. Batsouli,⁴³ V. Baublis,⁴⁶ C. Baumann,³⁷ A. Bazilevsky,⁶ S. Belikov,^{6,*} R. Bennett,⁵⁴ A. Berdnikov,⁵⁰ Y. Berdnikov,⁵⁰ A. A. Bickley,¹¹ J. G. Boissevain,³³ H. Borel,¹⁴ K. Boyle,⁵⁴ M. L. Brooks,³³ H. Buesching,⁶ V. Bumazhnov,²¹ G. Bunce,^{6,48} S. Butsyk,^{33,54} C. M. Camacho,³³ S. Campbell,⁵⁴ B. S. Chang,⁶² W. C. Chang,² J.-L. Charvet,¹⁴ S. Chernichenko,²¹ J. Chiba,²⁶ C. Y. Chi,¹² M. Chiu,²² I. J. Choi,⁶² R. K. Choudhury,⁴ T. Chujo,^{58,59} P. Chung,⁵³ A. Churny,²¹ V. Cianciolo,⁴³ Z. Citron,⁵⁴ C. R. Clevén,¹⁹ B. A. Cole,¹² M. P. Comets,⁴⁴ P. Constantin,³³ M. Csanád,¹⁶ T. Csörgő,²⁷ T. Dahms,⁵⁴ S. Dairaku,^{30,47} K. Das,¹⁸ G. David,⁶ M. B. Deaton,¹ K. Dehmelt,¹⁷ H. Delagrange,⁵⁵ A. Denisov,²¹ D. d'Enterria,^{12,31} A. Deshpande,^{48,54} E. J. Desmond,⁶ O. Dietzsch,⁵¹ A. Dion,⁵⁴ M. Donadelli,⁵¹ O. Drapier,³¹ A. Drees,⁵⁴ K. A. Drees,⁵ A. K. Dubey,⁶¹ A. Durum,²¹ D. Dutta,⁴ V. Dzordzhadze,⁷ Y. V. Efremenko,⁴³ J. Egdemir,⁵⁴ F. Ellinghaus,¹¹ W. S. Emam,⁷ T. Engelmöre,¹² A. Enokizono,³² H. En'yo,^{47,48} S. Esumi,⁵⁸ K. O. Eyser,⁷ B. Fadern,³⁸ D. E. Fields,^{41,48} M. Finger, Jr.,^{8,25} M. Finger,^{8,25} F. Fleuret,³¹ S. L. Fokin,²⁹ Z. Fraenkel,^{61,*} J. E. Frantz,⁵⁴ A. Franz,⁶ A. D. Frawley,¹⁸ K. Fujiwara,⁴⁷ Y. Fukao,^{30,47} T. Fusayasu,⁴⁰ S. Gadrat,³⁴ I. Garishvili,⁵⁶ A. Glenn,¹¹ H. Gong,⁵⁴ M. Gonin,³¹ J. Gosset,¹⁴ Y. Goto,^{47,48} R. Granier de Cassagnac,³¹ N. Grau,^{12,24} S. V. Greene,⁵⁹ M. Grosse Perdekamp,^{22,48} T. Gunji,¹⁰ H. -Å. Gustafsson,^{35,*} T. Hachiya,²⁰ A. Hadj Henni,⁵⁵ C. Haegemann,⁴¹ J. S. Haggerty,⁶ H. Hamagaki,¹⁰ R. Han,⁴⁵ H. Harada,²⁰ E. P. Hartouni,³² K. Haruna,²⁰ E. Haslum,³⁵ R. Hayano,¹⁰ M. Heffner,³² T. K. Hemmick,⁵⁴ T. Hester,⁷ X. He,¹⁹ H. Hiejima,²² J. C. Hill,²⁴ R. Hobbs,⁴¹ M. Hohlmann,¹⁷ W. Holzmann,⁵³ K. Homma,²⁰ B. Hong,²⁸ T. Horaguchi,^{10,47,57} D. Hornback,⁵⁶ S. Huang,⁵⁹ T. Ichihara,^{47,48} R. Ichimiya,⁴⁷ H. Iinuma,^{30,47} Y. Ikeda,⁵⁸ K. Imai,^{30,47} J. Imrek,¹⁵ M. Inaba,⁵⁸ Y. Inoue,^{49,47} D. Isenhowe,¹ L. Isenhowe,¹ M. Ishihara,⁴⁷ T. Isobe,¹⁰ M. Issah,⁵³ A. Isupov,²⁵ D. Ivanishev,⁴⁶ B. V. Jacak,^{54,†} J. Jia,¹² J. Jin,¹² O. Jinnouchi,⁴⁸ B. M. Johnson,⁶ K. S. Joo,³⁹ D. Jouan,⁴⁴ F. Kajihara,¹⁰ S. Kametani,^{10,47,60} N. Kamihara,^{47,48} J. Kamin,⁵⁴ M. Kaneta,⁴⁸ J. H. Kang,⁶² H. Kanou,^{47,57} J. Kapustinsky,³³ D. Kawall,^{36,48} A. V. Kazantsev,²⁹ T. Kempel,²⁴ A. Khanzadeev,⁴⁶ K. M. Kijima,²⁰ J. Kikuchi,⁶⁰ B. I. Kim,²⁸ D. H. Kim,³⁹ D. J. Kim,⁶² E. Kim,⁵² S. H. Kim,⁶² E. Kinney,¹¹ K. Kiriluk,¹¹ Á. Kiss,¹⁶ E. Kistenev,⁶ A. Kiyomichi,⁴⁷ J. Klay,³² C. Klein-Boesing,³⁷ L. Kochenda,⁴⁶ V. Kochetkov,²¹ B. Komkov,⁴⁶ M. Konno,⁵⁸ J. Koster,²² D. Kotchetkov,⁷ A. Kozlov,⁶¹ A. Král,¹³ A. Kravitz,¹² J. Kubart,^{8,23} G. J. Kunde,³³ N. Kurihara,¹⁰ K. Kurita,^{49,47} M. Kurosawa,⁴⁷ M. J. Kweon,²⁸ Y. Kwon,^{56,62} G. S. Kyle,⁴² R. Lacey,⁵³ Y. S. Lai,¹² J. G. Lajoie,²⁴ D. Layton,²² A. Lebedev,²⁴ D. M. Lee,³³ K. B. Lee,²⁸ M. K. Lee,⁶² T. Lee,⁵² M. J. Leitch,³³ M. A. L. Leite,⁵¹ B. Lenzi,⁵¹ P. Liebing,⁴⁸ T. Liška,¹³ A. Litvinenko,²⁵ H. Liu,⁴² M. X. Liu,³³ X. Li,⁹ B. Love,⁵⁹ D. Lynch,⁶ C. F. Maguire,⁵⁹ Y. I. Makdisi,⁵ A. Malakhov,²⁵ M. D. Malik,⁴¹ V. I. Manko,²⁹ E. Mannel,¹² Y. Mao,^{45,47} L. Mašek,^{8,23} H. Masui,⁵⁸ F. Matathias,¹² M. McCumber,⁵⁴ P. L. McGaughey,³³ N. Means,⁵⁴ B. Meredith,²² Y. Miake,⁵⁸ P. Mikeš,^{8,23} K. Miki,⁵⁸ T. E. Miller,⁵⁹ A. Milov,^{6,54} S. Mioduszewski,⁶ M. Mishra,³ J. T. Mitchell,⁶ M. Mitrovski,⁵³ A. K. Mohanty,⁴ Y. Morino,¹⁰ A. Morreale,⁷ D. P. Morrison,⁶ T. V. Moukhanova,²⁹ D. Mukhopadhyay,⁵⁹ J. Murata,^{49,47} S. Nagamiya,²⁶ Y. Nagata,⁵⁸ J. L. Nagle,¹¹ M. Naglis,⁶¹ M. I. Nagy,¹⁶ I. Nakagawa,^{47,48} Y. Nakamiya,²⁰ T. Nakamura,²⁰ K. Nakano,^{47,57} J. Newby,³² M. Nguyen,⁵⁴ T. Niita,⁵⁸ B. E. Norman,³³ R. Nouicer,⁶ A. S. Nyanin,²⁹ E. O'Brien,⁶ S. X. Oda,¹⁰ C. A. Ogilvie,²⁴ H. Ohnishi,⁴⁷ K. Okada,⁴⁸ M. Oka,⁵⁸ O. O. Omiwade,¹ Y. Onuki,⁴⁷ A. Oskarsson,³⁵ M. Ouchida,²⁰ K. Ozawa,¹⁰ R. Pak,⁶ D. Pal,⁵⁹ A. P. T. Palounek,³³ V. Pantuev,⁵⁴ V. Papavassiliou,⁴² J. Park,⁵² W. J. Park,²⁸ S. F. Pate,⁴² H. Pei,²⁴ J.-C. Peng,²² H. Pereira,¹⁴ V. Peresedov,²⁵ D. Yu. Peressouko,²⁹ C. Pinkenburg,⁶ M. L. Purschke,⁶ A. K. Purwar,³³ H. Qu,¹⁹ J. Rak,⁴¹ A. Rakotozafindrabe,³¹ I. Ravinovich,⁶¹ K. F. Read,^{43,56} S. Rembeczki,¹⁷ M. Reuter,⁵⁴ K. Reygers,³⁷ V. Riabov,⁴⁶ Y. Riabov,⁴⁶ D. Roach,⁵⁹ G. Roche,³⁴ S. D. Rolnick,⁷ A. Romana,^{31,*} M. Rosati,²⁴ S. S. E. Rosendahl,³⁵ P. Rosnet,³⁴ P. Rukoyatkin,²⁵ P. Ružička,²³ V. L. Rykov,⁴⁷ B. Sahlmueller,³⁷ N. Saito,^{30,47,48} T. Sakaguchi,⁶ S. Sakai,⁵⁸ K. Sakashita,^{47,57} H. Sakata,²⁰ V. Samsonov,⁴⁶ S. Sato,²⁶ T. Sato,⁵⁸ S. Sawada,²⁶ K. Sedgwick,⁷ J. Seele,¹¹ R. Seidl,²² A. Yu. Semenov,²⁴ V. Semenov,²¹ R. Seto,⁷ D. Sharma,⁶¹ I. Shein,²¹ A. Shevel,^{46,53} T.-A. Shibata,^{47,57} K. Shigaki,²⁰ M. Shimomura,⁵⁸ K. Shoji,^{30,47} P. Shukla,⁴ A. Sickles,^{6,54} C. L. Silva,⁵¹ D. Silvermyr,⁴³ C. Silvestre,¹⁴ K. S. Sim,²⁸ B. K. Singh,³ C. P. Singh,³ V. Singh,³ S. Skutnik,²⁴ M. Slunečka,^{8,25} A. Soldatov,²¹ R. A. Soltz,³² W. E. Sondheim,³³ S. P. Sorensen,⁵⁶ I. V. Sourikova,⁶ F. Staley,¹⁴ P. W. Stankus,⁴³ E. Stenlund,³⁵ M. Stepanov,⁴² A. Ster,²⁷ S. P. Stoll,⁶ T. Sugitate,²⁰ C. Suire,⁴⁴ A. Sukhanov,⁶ J. Sziklai,²⁷ T. Tabaru,⁴⁸ S. Takagi,⁵⁸ E. M. Takagui,⁵¹ A. Taketani,^{47,48} R. Tanabe,⁵⁸ Y. Tanaka,⁴⁰ K. Tanida,^{47,48,52} M. J. Tannenbaum,⁶ A. Taranenko,⁵³ P. Tarján,¹⁵ H. Themann,⁵⁴

T. L. Thomas,⁴¹ M. Togawa,^{30,47} A. Toia,⁵⁴ J. Tojo,⁴⁷ L. Tomášek,²³ Y. Tomita,⁵⁸ H. Torii,^{20,47} R. S. Towell,¹ V.-N. Tram,³¹ I. Tserruya,⁶¹ Y. Tsuchimoto,²⁰ C. Vale,²⁴ H. Valle,⁵⁹ H. W. van Hecke,³³ A. Veicht,²² J. Velkovska,⁵⁹ R. Vértési,¹⁵ A. A. Vinogradov,²⁹ M. Virius,¹³ V. Vrba,²³ E. Vznuzdaev,⁴⁶ M. Wagner,^{30,47} D. Walker,⁵⁴ X. R. Wang,⁴² Y. Watanabe,^{47,48} F. Wei,²⁴ J. Wessels,³⁷ S. N. White,⁶ D. Winter,¹² C. L. Woody,⁶ M. Wysocki,¹¹ W. Xie,⁴⁸ Y. L. Yamaguchi,⁶⁰ K. Yamaura,²⁰ R. Yang,²² A. Yanovich,²¹ Z. Yasin,⁷ J. Ying,¹⁹ S. Yokkaichi,^{47,48} G. R. Young,⁴³ I. Younus,⁴¹ I. E. Yushmanov,²⁹ W. A. Zajc,¹² O. Zaudtke,³⁷ C. Zhang,⁴³ S. Zhou,⁹ J. Zimányi,^{27,*} and L. Zolin²⁵

(PHENIX Collaboration)

¹Abilene Christian University, Abilene, Texas 79699, USA

²Institute of Physics, Academia Sinica, Taipei 11529, Taiwan

³Department of Physics, Banaras Hindu University, Varanasi 221005, India

⁴Bhabha Atomic Research Centre, Bombay 400 085, India

⁵Collider-Accelerator Department, Brookhaven National Laboratory, Upton, New York 11973-5000, USA

⁶Physics Department, Brookhaven National Laboratory, Upton, New York 11973-5000, USA

⁷University of California–Riverside, Riverside, California 92521, USA

⁸Charles University, Ovocný trh 5, Praha 1, 116 36, Prague, Czech Republic

⁹Science and Technology on Nuclear Data Laboratory, China Institute of Atomic Energy, Beijing, People's Republic of China

¹⁰Center for Nuclear Study, Graduate School of Science, University of Tokyo, 7-3-1 Hongo, Bunkyo, Tokyo 113-0033, Japan

¹¹University of Colorado, Boulder, Colorado 80309, USA

¹²Columbia University, New York, New York 10027 and Nevis Laboratories, Irvington, New York 10533, USA

¹³Czech Technical University, Zikova 4, 166 36 Prague 6, Czech Republic

¹⁴Dapnia, CEA Saclay, F-91191, Gif-sur-Yvette, France

¹⁵Debrecen University, H-4010 Debrecen, Egyetem tér 1, Hungary

¹⁶ELTE, Eötvös Loránd University, H-1117 Budapest, Pázmány P.s. 1/A, Hungary

¹⁷Florida Institute of Technology, Melbourne, Florida 32901, USA

¹⁸Florida State University, Tallahassee, Florida 32306, USA

¹⁹Georgia State University, Atlanta, Georgia 30303, USA

²⁰Hiroshima University, Kagamiyama, Higashi-Hiroshima 739-8526, Japan

²¹IHEP Protvino, State Research Center of Russian Federation, Institute for High Energy Physics, Protvino, 142281, Russia

²²University of Illinois at Urbana-Champaign, Urbana, Illinois 61801, USA

²³Institute of Physics, Academy of Sciences of the Czech Republic, Na Slovance 2, 182 21 Prague 8, Czech Republic

²⁴Iowa State University, Ames, Iowa 50011, USA

²⁵Joint Institute for Nuclear Research, 141980 Dubna, Moscow Region, Russia

²⁶KEK, High Energy Accelerator Research Organization, Tsukuba, Ibaraki 305-0801, Japan

²⁷KFKI Research Institute for Particle and Nuclear Physics of the Hungarian Academy of Sciences (MTA KFKI RMKI), H-1525 Budapest 114, P.O. Box 49, Budapest, Hungary

²⁸Korea University, Seoul, 136-701, Korea

²⁹Russian Research Center “Kurchatov Institute”, Moscow, Russia

³⁰Kyoto University, Kyoto 606-8502, Japan

³¹Laboratoire Leprince-Ringuet, Ecole Polytechnique, CNRS-IN₂P₃, Route de Saclay, F-91128, Palaiseau, France

³²Lawrence Livermore National Laboratory, Livermore, California 94550, USA

³³Los Alamos National Laboratory, Los Alamos, New Mexico 87545, USA

³⁴LPC, Université Blaise Pascal, CNRS-IN₂P₃, Clermont-Fd, 63177 Aubiere Cedex, France

³⁵Department of Physics, Lund University, Box 118, SE-221 00 Lund, Sweden

³⁶Department of Physics, University of Massachusetts, Amherst, Massachusetts 01003-9337, USA

³⁷Institut für Kernphysik, University of Muenster, D-48149 Muenster, Germany

³⁸Muhlenberg College, Allentown, Pennsylvania 18104-5586, USA

³⁹Myongji University, Yongin, Kyonggido 449-728, Korea

⁴⁰Nagasaki Institute of Applied Science, Nagasaki-shi, Nagasaki 851-0193, Japan

⁴¹University of New Mexico, Albuquerque, New Mexico 87131, USA

⁴²New Mexico State University, Las Cruces, New Mexico 88003, USA

⁴³Oak Ridge National Laboratory, Oak Ridge, Tennessee 37831, USA

⁴⁴IPN-Orsay, Université Paris Sud, CNRS-IN₂P₃, BP1, F-91406, Orsay, France

⁴⁵Peking University, Beijing, People's Republic of China

⁴⁶PNPI, Petersburg Nuclear Physics Institute, Gatchina, Leningrad region, 188300, Russia

⁴⁷RIKEN Nishina Center for Accelerator-Based Science, Wako, Saitama 351-0198, JAPAN

⁴⁸RIKEN BNL Research Center, Brookhaven National Laboratory, Upton, New York 11973-5000, USA

⁴⁹Physics Department, Rikkyo University, 3-34-1 Nishi-Ikebukuro, Toshima, Tokyo 171-8501, Japan

⁵⁰*Saint Petersburg State Polytechnic University, St. Petersburg, Russia*⁵¹*Universidade de São Paulo, Instituto de Física, Caixa Postal 66318, São Paulo CEP05315-970, Brazil*⁵²*System Electronics Laboratory, Seoul National University, Seoul, Korea*⁵³*Chemistry Department, Stony Brook University, Stony Brook, SUNY, New York 11794-3400, USA*⁵⁴*Department of Physics and Astronomy, Stony Brook University, SUNY, Stony Brook, New York 11794, USA*⁵⁵*SUBATECH (Ecole des Mines de Nantes, CNRS-IN2P3, Université de Nantes) BP 20722 - 44307, Nantes, France*⁵⁶*University of Tennessee, Knoxville, Tennessee 37996, USA*⁵⁷*Department of Physics, Tokyo Institute of Technology, Oh-okayama, Meguro, Tokyo 152-8551, Japan*⁵⁸*Institute of Physics, University of Tsukuba, Tsukuba, Ibaraki 305, Japan*⁵⁹*Vanderbilt University, Nashville, Tennessee 37235, USA*⁶⁰*Waseda University, Advanced Research Institute for Science and Engineering, 17 Kikui-cho, Shinjuku-ku, Tokyo 162-0044, Japan*⁶¹*Weizmann Institute, Rehovot 76100, Israel*⁶²*Yonsei University, IPAP, Seoul 120-749, Korea*

(Received 20 May 2010; published 16 March 2011)

The PHENIX experiment at the Relativistic Heavy Ion Collider has measured the invariant differential cross section for production of K_S^0 , ω , η' , and ϕ mesons in $p + p$ collisions at $\sqrt{s} = 200$ GeV. Measurements of ω and ϕ production in different decay channels give consistent results. New results for the ω are in agreement with previously published data and extend the measured p_T coverage. The spectral shapes of all hadron transverse momentum distributions measured by PHENIX are well described by a Tsallis distribution functional form with only two parameters, n and T , determining the high- p_T and characterizing the low- p_T regions of the spectra, respectively. The values of these parameters are very similar for all analyzed meson spectra, but with a lower parameter T extracted for protons. The integrated invariant cross sections calculated from the fitted distributions are found to be consistent with existing measurements and with statistical model predictions.

DOI: [10.1103/PhysRevD.83.052004](https://doi.org/10.1103/PhysRevD.83.052004)

PACS numbers: 25.75.Dw

I. INTRODUCTION

The PHENIX experiment at the Relativistic Heavy Ion Collider (RHIC) at Brookhaven National Laboratory has measured the production of a wide variety of hadrons (π , K , η , η' , ω , ϕ , p , J/ψ , and ψ') at midrapidity in $p + p$ collisions at $\sqrt{s} = 200$ GeV. The measurements were performed using a time-of-flight technique for charged hadron identification and via reconstruction of various photonic, hadronic, and dielectron decay modes for neutral hadrons. The measured transverse momentum spectra extend over the range from zero to 20 GeV/ c . Precise measurements of hadron production in $p + p$ collisions are crucial for a deeper understanding of QCD phenomena such as parton dynamics and hadronization. They also provide a valuable baseline for particle and jet production in heavy ion collisions, essential to the needs of the RHIC heavy ion program.

There exists a large body of experimental data on hadron production in $p + p$ collisions measured at the Intersecting Storage Rings, $S\bar{p}\bar{p}S$, Tevatron, and RHIC [1–19]. At high p_T the spectra display a power law behavior that becomes more and more evident as the interaction energy increases. In this regime, the spectra are well described by perturbative QCD together with measured proton structure func-

tions [20]. At low p_T , typically $p_T < 2$ GeV/ c , a region which accounts for the bulk of the produced particles, the spectra are governed by processes that belong to the non-perturbative regime of QCD and are not yet fully understood. In this p_T region, the spectra reveal an exponential behavior which can be explained with the assumption that secondary particles are emitted from a thermalized system with, at most, short-range correlations and obeying Boltzmann-Gibbs statistics [21]. In this approach, the inverse slope parameter T can be interpreted as the temperature of the system. However, that would require some mechanism of local thermal equilibrium in $p + p$ collisions which is not yet established. It is also known that the particle spectra are best described by an exponential in m_T rather than in p_T [22]. According to the observation that the temperature parameter T in the exponential function is the same for different particles, the spectral shape is also the same. This observation is consistent with m_T scaling [18,23].

The two regimes described here and the p_T region where their contributions are predominant are commonly designated as “soft” and “hard.” There is no obvious boundary between them, and the distinction between production mechanisms in each region is difficult to determine experimentally. The spectral shapes of all hadrons produced in $p + p$ collisions at $\sqrt{s} = 200$ GeV are well described by one single distribution without making a distinct division into two regions. The Tsallis [24] distribution, also referred to as a Levy distribution [7,25], has only two parameters, T

*Deceased.

†PHENIX Spokesperson.
jacak@skipper.physics.sunysb.edu

and n , that characterize the low- and high- p_T regions of the spectra, respectively. This distribution has been shown by Tsallis to result from a postulated generalization of the Boltzmann-Gibbs entropy. It has been suggested to be relevant for various types of systems, such as those with long-range correlations, or nonergodic filling of the available phase space. Boltzmann statistics and exponential distributions are recovered in the limit that correlations disappear. The parameter T then recovers the usual interpretation as the temperature of the system.

In a number of recent publications [26–30] the Tsallis statistical distribution was successfully applied to describe data for $A + A$ and $p + p$ collisions over a wide range of incident energies and centralities. Discussed in other publications [31–36] are the physical mechanisms responsible for the successful application of the nonextensive statistical approach to the description of the particle spectra. However, the analysis presented in this paper uses the Tsallis formalism primarily as a parametrization to describe the particle spectra and compares it with other parametrizations used for the spectra approximation. Common features and differences revealed in such an approach are data driven and should contribute to a better understanding of particle production mechanisms.

The successful description of the particle spectra with the Tsallis distribution allows us to accurately calculate the integrated particle yield and mean momentum, even for species measured only in a limited momentum range. The integrated particle abundances provide important information on the bulk properties of the soft particle production. In particular, the comparison of the particle yields to statistical model predictions can be used to infer the degree of hadro-chemical equilibration. In the case of heavy ion collisions, the success of statistical model fits to the particle yields [37,38] suggests that hadro-chemical equilibration is essentially complete. These models have also been used to describe particle production in $p + p$ collisions [39,40].

In this paper we present new PHENIX results on the production of neutral mesons in $p + p$ collisions at $\sqrt{s} = 200$ GeV and compare the PHENIX data with the parametrizations commonly used to describe particle spectra in relativistic $p + p$ collisions, including the Tsallis parametrization. It is demonstrated that the latter describes the data in the entire range of measured p_T most accurately. The parameter values extracted from the fits are given for all measured particles.

The paper is organized as follows: Sec. II gives a description of the PHENIX experimental setup and detector subsystems. Section III describes the analysis methods used to measure the transverse momentum spectra of different hadrons for $p + p$ collisions at $\sqrt{s} = 200$ GeV. In Sec. IV the properties of the measured transverse momentum spectra are analyzed. In Sec. V the scaling properties of the particle spectra are discussed and the calculated

integrated yields are compared with published results and with statistical model calculations. The measured invariant cross sections are tabulated in tables given in the Appendix.

II. PHENIX DETECTOR

The PHENIX detector is designed as a high rate and fine granularity apparatus that utilizes a variety of detector technologies to measure global characteristics of the events, and to measure leptons, hadrons, and photons over a wide range of transverse momenta. The experimental setup comprises two central arm spectrometers each covering $\Delta\phi = \pi/2$ in azimuth at midrapidity $|\eta| < 0.35$, and two forward muon spectrometers with full azimuthal coverage in the rapidity interval $1.2 < |\eta| < 2.4(2.2)$ for the north (south) arm and a system of “global” detectors. Each spectrometer provides very good momentum and spatial resolution and particle identification capabilities. The detailed description of the detector can be found elsewhere [41]. The experimental results presented in this paper were obtained using the central spectrometers and global detectors of the PHENIX experiment schematically shown in Fig. 1.

Reconstruction of charged particle tracks and momentum measurements are performed with the drift chambers (DC) and the first layer of the pad chambers (PC1). The fiducial volume of the DC is located outside of the analyzing magnetic field of the detector and has an inner radius of 2.02 m and an outer radius of 2.46 m. Multiple layers of wires measure the track position with an angular resolution of ~ 0.8 mrad in the bending plane perpendicular to the beam axis. The PC1, located just outside the outer radius of the DC, has a spatial resolution of $\sigma_\phi \sim 2.4$ mm and $\sigma_z \sim 1.7$ mm and provides the z coordinate of the track at the

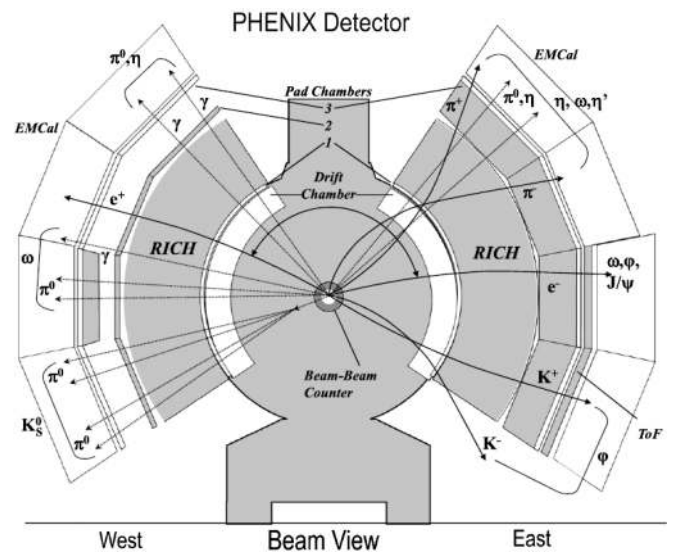


FIG. 1. Schematic view of the PHENIX central spectrometers and particle decay modes analyzed in this paper.

exit of the DC. The momentum of a particle is determined by the measured bending angle in the axial magnetic field of the central magnet [42], assuming that the particle originates from the collision vertex. The DC momentum resolution is estimated to be $\delta p/p = 0.7 \oplus 1.1\% p$ [GeV/ c]. Track matching with hits in the second (PC2) and third (PC3) pad chamber layers located at radii of 4.2 m and 5.0 m, respectively, rejects tracks from secondaries originating either from decays of long-lived hadrons or from interactions with the structure of the detector. Such tracks have not passed through the full magnetic field and therefore have improperly determined momenta that are typically overestimated. A detailed description of the PHENIX tracking system can be found in [43,44].

The primary purpose of the PHENIX electromagnetic calorimeter (EMCal) is to measure the position and energy of photons and electrons. The EMCal covers the full acceptance of the central spectrometers and is divided into eight sectors. Six of the EMCal sectors located at a radius of 5.0 m are built of lead scintillator (PbSc) and comprise 15 552 individual towers with a granularity of 5.5×5.5 cm² and a depth of $18 X_0$. The two other sectors located at a radius of 5.2 m are built of lead glass (PbGl) and comprise 9216 lead-glass Čerenkov towers with a granularity of 4×4 cm² and a depth of $14.4 X_0$. Because of the fine segmentation of the EMCal, the electromagnetic showers typically spread over several towers. This spread provides the means to analyze the position and shape of the shower, and to reject hadrons which produce showers of a different shape. The spatial resolution of the PbSc (PbGl) EMCal sector is $\sigma(E) = 1.55(0.2) \oplus 5.7(8.4)/\sqrt{E[\text{GeV}]}$ mm for particles at normal incidence. The energy resolution of the PbSc (PbGl) calorimeter is $\delta E/E = 2.1(0.8)\% \oplus 8.1(5.9)/\sqrt{E[\text{GeV}]}\%$.

The time-of-flight (TOF) subsystem is used for hadron identification based on momentum measurements in the DC and PC1 combined with flight path length from the collision vertex [45]. The TOF is located between the PC3 and the PbGl at a radius of 5.0 m and covers about 1/3 of the acceptance of one central arm. The TOF detector comprises 10 panels, each containing 96 segments equipped with plastic scintillators and photomultiplier readout from both ends. The time resolution of ~ 120 ps enables π/K and K/p separation in the transverse momentum ranges 0.3–2.5 GeV/ c and 0.3–5.0 GeV/ c , respectively. The lower limit is defined by the energy loss of different particles in the detector material.

The Ring-Imaging Čerenkov (RICH) detector is the primary detector for e/π separation. It provides an e/π rejection factor of $\sim 10^{-3}$ for tracks with momenta below the pion Čerenkov threshold of ~ 4 GeV/ c in the CO₂ used as a radiator gas. The RICH detector, in each arm, has a mirror measuring 20 m² that focuses the light onto an array of 2560 photomultipliers. The material of the PHENIX central arm that precedes the RICH detector has been kept to just $\sim 2\%$ of a radiation length in order

to minimize the background contribution of electrons from γ conversion. The PHENIX RICH and TOF detectors are described in more detail in [45].

The Beam-Beam Counter (BBC) detectors [46] are used for triggering, determination of the collision time, and location of the vertex along the beam axis, z_{vtx} . Each BBC comprises 64 Čerenkov counters surrounding the beam pipe, and located at a distance of ± 1.44 m from the center of the interaction region. Each BBC covers the full azimuth and the pseudorapidity interval $3.1 < |\eta| < 3.9$. The z coordinate of the collision vertex is determined with a typical resolution of 2 cm in $p + p$ collisions by the timing difference of the signals from each BBC. The time average of all BBC signals gives a start time for the time-of-flight measurements. The minimum bias trigger in $p + p$ collisions is generated when there is at least one count from each BBC, and the collision vertex calculated online is $|z_{\text{vtx}}| < 38$ cm. The efficiency of the minimum bias trigger is estimated to be $(55 \pm 5)\%$ of the total inelastic cross section of $\sigma_{\text{inel}}^{pp} = 42 \pm 3$ mb. Further details about the BBC subsystem of the PHENIX detector can be found in [46].

Because of the high rate of $p + p$ collisions at RHIC, PHENIX employs several specialized triggers which enable the experiment to sample more of the delivered luminosity for rare events. Besides the minimum bias trigger, the experimental results presented in this paper were obtained using the EMCal-RICH Trigger (ERT).

The EMCal is used to trigger on rare events with a large energy deposit originating primarily from high-energy photons or electrons. The analog sum of signals from 4×4 adjacent towers is compared with a trigger threshold of 1.4 GeV. In addition, a combination of the EMCal and the RICH signals is used to build the ERT trigger, which is designed to select events containing electrons. The trigger fires when the analog sum of signals from 2×2 adjacent towers in the EMCal exceeds a threshold of 0.4 GeV (setting used in the 2005 physics run) or 0.6 GeV (used in 2006) in geometrical coincidence with a signal in the associated RICH trigger tile (4×5 PMTs) determined using a lookup table.

III. NEUTRAL MESON MEASUREMENTS

In this section we describe the analysis details of the $K_S^0 \rightarrow \pi^0 \pi^0$, $\omega \rightarrow \pi^0 \pi^+ \pi^-$, $\omega \rightarrow \pi^0 \gamma$, $\omega \rightarrow e^+ e^-$, $\eta^0 \rightarrow \eta \pi^+ \pi^-$, $\phi \rightarrow K^+ K^-$, and $\phi \rightarrow e^+ e^-$ measurements in $p + p$ collisions at $\sqrt{s} = 200$ GeV. These measurements complete and extend previous neutral meson spectra results measured by the PHENIX experiment and published in [2,3,5,6,47,48].

The measurements are based on a data sample representing a total integrated luminosity of 2.5 pb^{-1} within a vertex cut of $|z_{\text{vtx}}| < 30$ cm accumulated by the PHENIX experiment in 2005. The data were collected using minimum bias and ERT triggers.

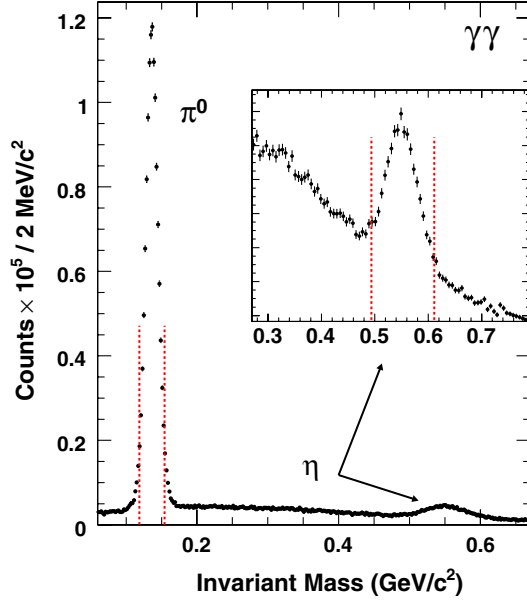


FIG. 2 (color online). Invariant mass distribution for $\gamma\gamma$ pairs in the range $4 < p_T$ (GeV/c) < 6 . The inset shows an enlargement of the region around the η mass.

A. Reconstruction of neutral mesons

Here we discuss the analysis details and main parameters of the invariant mass distributions reconstructed for different decay modes.

1. Selection of the π^0 , $\eta \rightarrow \gamma\gamma$ candidates

Most particles studied in this section decay, producing a π^0 or η meson in the final state, which in turn decays into a $\gamma\gamma$ pair at the point of primary decay. The analysis procedures for the measurement of the inclusive π^0 and η invariant transverse momentum spectra in $p + p$ collisions have been published previously [2,3,6,47]. Meson candidates were reconstructed from pairs of clusters in the

EMCal with energy $E_\gamma > 0.2$ GeV, assuming that they correspond to photons originating from the collision vertex. A shower profile cut was used to reject broader showers predominantly produced by hadrons [49]. The invariant mass distribution for cluster pairs is shown in Fig. 2.

The width of the peaks is determined largely by the EMCAL energy resolution. For $\pi^0(\eta)$ meson candidates the width decreases from 12(40) MeV/ c^2 to 9(30) MeV/ c^2 between 1 GeV/ c and 3 GeV/ c of the pair transverse momentum.

The reconstructed positions and widths of the peaks are in agreement with simulation results once detector resolution and trigger biases have been taken into account. The measured mass peaks were parametrized as a function of the $\gamma\gamma$ pair p_T . For further analyses involving π^0 or η mesons in the final state, we selected pairs with $p_T > 1$ GeV/ c and an invariant mass within 2 standard deviations of the measured peak position. All $\gamma\gamma$ pairs satisfying these criteria were assigned the nominal mass of the meson [50] and the photon energies were rescaled by the ratio of the nominal to the reconstructed masses.

2. $\omega \rightarrow \pi^0\gamma$ and $K_S^0 \rightarrow \pi^0\pi^0$

The reconstruction of $\omega \rightarrow \pi^0\gamma$ and $K_S^0 \rightarrow \pi^0\pi^0$ decays was performed by combining π^0 candidates with either all other photons with energy $E_\gamma > 1$ GeV [4] or with all other π^0 candidates from the same event. Combinations using the same EMCAL clusters more than once were rejected.

Invariant mass distributions for $\pi^0\gamma$ and $\pi^0\pi^0$ decays are shown in Fig. 3. The width of the ω meson peak is ~ 30 MeV and has a weak p_T dependence. The width of the K_S^0 peak is ~ 15 MeV. The signal-to-background ratio (S:B) increases from 1:30 (1:4) to 1:5 (1:2) for ω (K_S^0) mesons as the transverse momentum increases from 2 to 12 GeV/ c .

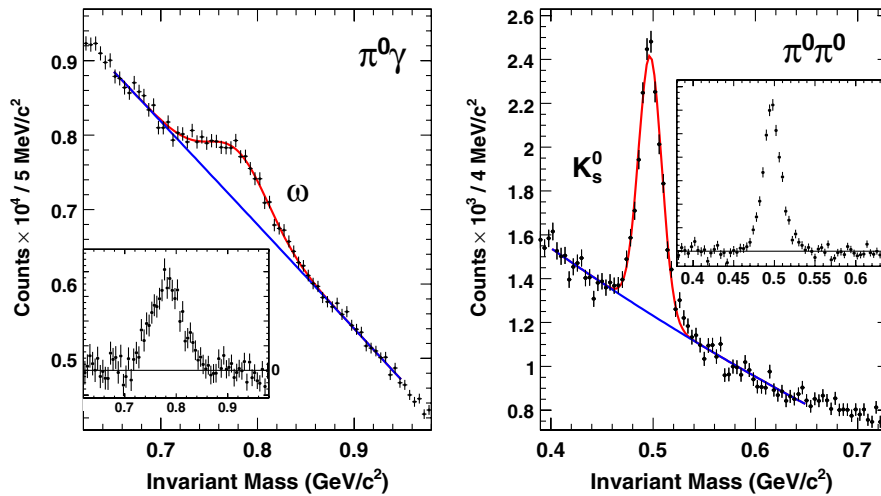


FIG. 3 (color online). Invariant mass distribution for $\pi^0\gamma$ (left panel) and $\pi^0\pi^0$ (right panel) decays at $4 < p_T$ (GeV/c) < 6 .

The main difference in the analysis of the ω and K_S^0 decays was due to the large lifetime of the K_S^0 meson. Neutral pions coming from the decays of high- p_T K_S^0 originate from a displaced vertex, and their reconstructed mass and width need to be parametrized in a different way compared to pions coming from the primary event vertex. This effect was studied using the PHENIX Monte Carlo calculations. The correction was based on the mass and width of π^0 's coming from kaon decays with a realistic p_T distribution, and on π^0 's produced at the collision vertex with the inclusive p_T distribution.

3. $\omega, \eta \rightarrow \pi^0 \pi^+ \pi^-$, $\eta' \rightarrow \eta \pi^+ \pi^-$

For the reconstruction of $\omega, \eta \rightarrow \pi^0 \pi^+ \pi^-$ and $\eta' \rightarrow \eta \pi^+ \pi^-$ decay modes, we combined $\pi^0(\eta)$ candidates with all pairs of oppositely charged tracks in the same event [2,4]. Charged tracks accepted for this analysis were required to have momenta in the range $0.2 < p_T$ (GeV/c) < 8 , and were assigned the charged pion mass. Tracks with momentum below 0.2 GeV/c do not go through the entire detector due to their large bending angle in the axial magnetic field of the central magnet. Tracks that appear to have momenta above 8 GeV/c are, for the most part, low momentum secondaries coming from the decay of long-lived primaries. Because they do not originate from the collision vertex, their momenta are not calculated correctly. Invariant mass distributions for $\pi^0(\eta)\pi^+\pi^-$ triples are shown in Fig. 4. The two peaks in the distribution shown in the left panel correspond to decays of η and ω mesons. The width of ~ 8 MeV/ c^2 for the reconstructed η meson peak is similar to that of the η' meson peak shown in the right panel of Fig. 4. The width of the ω -meson peak is ~ 17 MeV/ c^2 , which is narrower than that in the $\omega \rightarrow \pi^0 \gamma$ decay mode. This is due to the smaller difference between the masses of the primary particle and their decay products and to the better momentum

resolution of the tracking system as compared to the EMCAL in this momentum range. The signal-to-background ratio in the range of measurements changes from 1:10 (1:5) to 1:3 (1:2) for ω (η') mesons. More details on the analysis of η and ω mesons can be found in [2,4].

4. $\phi \rightarrow K^+ K^-$

Reconstruction of the $\phi \rightarrow K^+ K^-$ decay was done by combining pairs of oppositely charged tracks. The tracks were required to have a momentum in the range $0.3 < p_T$ (GeV/c) < 8 . Each track was assigned the charged kaon mass. Invariant mass distributions were accumulated in two different configurations: (i) combining all tracks reconstructed in the PHENIX tracking system and (ii) combining all tracks of one sign with tracks of the opposite sign identified as a kaon in the TOF subsystem. Examples of the invariant mass distributions for the two cases are shown in the left and right panels of Fig. 5, respectively.

The use of particle identification improved the signal-to-background ratio by a factor of more than 2 at the expense of a more limited acceptance, resulting in a factor of 5 loss in statistics. At low and intermediate p_T , where the combinatorial background is high but the data sample has large statistics, this method is preferable. The method without particle identification was more effective at intermediate and high p_T because of the significant gain in the acceptance. The highest p_T reachable with this method is limited by the available statistics in the minimum bias data sample. The two methods described here use different detector subsystems and produce different shapes of combinatorial background and signal-to-background ratios. Use of the two methods allowed us to extend the p_T coverage of the measurement and provided a consistency check between the results obtained in the overlap region between 1.5 GeV/c and 4.5 GeV/c. The signal-to-background

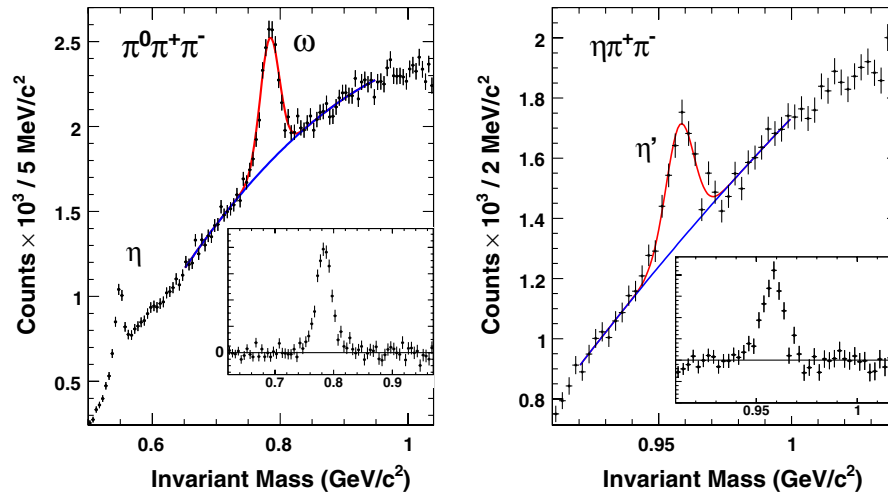


FIG. 4 (color online). Invariant mass distribution for $\pi^0 \pi^+ \pi^-$ (left panel) and $\eta \pi^+ \pi^-$ (right panel) triplets in the momentum range $4 < p_T$ (GeV/c) < 6 . The inset shows the invariant mass distribution after the background removal explained in Sec. III B.

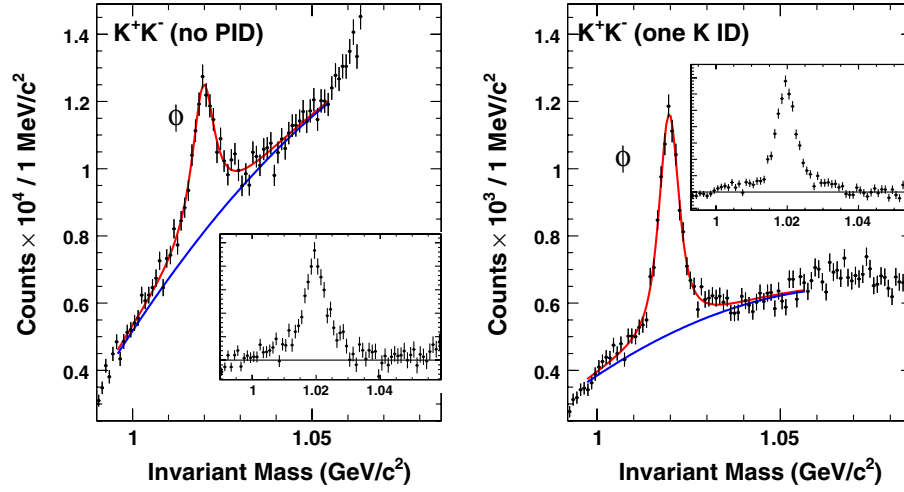


FIG. 5 (color online). Invariant mass distribution for K^+K^- accumulated without particle identification (left panel) and with one K -meson identification (right panel) in the momentum range $4 < p_T$ (GeV/ c) < 6 . The inset shows the invariant mass distribution after the background removal explained in Sec. III B.

ratio changes from 1:10 to 2:1 depending on the analysis method and the p_T bin. More details on this measurement can be found in [51].

5. ω , $\phi \rightarrow e^+e^-$

Electrons are reliably identified by the PHENIX detector in the momentum range $0.2 < p_T$ (GeV/ c) < 4 . Electron identification is accomplished using the information from the RICH and EMCal subsystems by requiring at least two RICH phototubes to fire within the ring-shaped area associated with a charged track. In addition, the ratio of the associated cluster energy measured in the EMCal to the momentum measured in the tracking system must satisfy $|E/p - 1| < 0.5$. The invariant mass distribution obtained by combining identified e^+ and e^- pairs is shown in Fig. 6

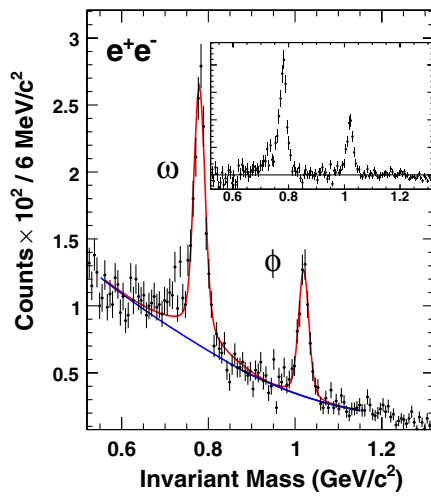


FIG. 6 (color online). Invariant mass distribution for e^+e^- pairs in the momentum range $0.5 < p_T$ (GeV/ c) < 0.75 . The inset shows the invariant mass distribution after the background removal explained in Sec. III B.

for pairs in the range $0.5 < p_T$ (GeV/ c) < 0.75 . The two peaks correspond to $\omega + \rho$ and ϕ mesons. The widths of the ω (ϕ) meson peaks vary from 6.1(6.0) MeV/ c^2 to 9.0(11) MeV/ c^2 , from the lowest p_T to the highest p_T of the electron pairs. The signal-to-background ratio in the region of the ω (ϕ) meson peaks changes from 1:2 (2:1) to 3:1 (6:1).

B. Raw yield extraction

To extract the raw yields the invariant mass distributions near each peak were parametrized as the sum of signal and background contributions.

For the signal, we used a Breit-Wigner function convolved with a Gaussian function (BW * G). The Breit-Wigner function describes the natural shape of the measured resonance, and the Gaussian takes into account the detector resolution. Depending on the decay channel being analyzed, one or the other contribution may dominate; e.g. the Gaussian part is more important in decays like $\omega \rightarrow \pi^0\gamma$ or $K_s^0 \rightarrow \pi^0\pi^0$, and the Breit-Wigner part in decays like $\phi \rightarrow K^+K^-$ or ω , $\phi \rightarrow e^+e^-$. In most cases the parameters of the BW * G function when fitted to the data were consistent with the values expected from simulation.

The $\phi \rightarrow K^+K^-$ decay mode was treated somewhat differently. Kaons decaying in flight before passing completely through the PHENIX tracking system modify the shape of the invariant mass distribution compared to those passing through the detector without decays. This results in non-Gaussian tails of the detector response function, and thus the Breit-Wigner and Gaussian width parameters in the BW * G convolution mix together. To account for this effect a Monte Carlo sample was produced with the natural width of the ϕ set to zero and the kaon lifetime set to infinity. Using these samples allowed us to disentangle the effects related to the kaon decays in flight.

Our analysis verified that the peak positions and widths obtained from the fits to the data were in agreement with the simulated values within the error bars. In the highest p_T bins, where the available statistics prevents unconstrained extraction of the Gaussian width from the data, we constrained the fitted width to be within 10% of the value found in the simulation. In the measurement of the ω , $\phi \rightarrow e^+e^-$ decays, other terms were added to the BW * G shape to account for ρ decays and for internal conversions taken from [52,53]. The contribution of ρ underneath the ω peak was estimated using Breit-Wigner parametrization, with the assumption that the production ratio of ρ and ω is 1; in the fit their ratio was determined by their e^+e^- branching ratios in vacuum equal to 1.53.

To properly estimate the background under the peak, it is necessary to assume that the shape of the background does not change rapidly. With this assumption one can expand the background shape in a Taylor series around the peak position and take the most significant terms of the expansion. A natural choice is to use a second order polynomial. The regions outside the resonance peak, where the background dominates, define the parameters of the fit. For a second order polynomial fit, the background varies smoothly under the peak. This may not be the case for higher order polynomial fits to the background.

The combinatorial background in the data has two main contributions. The first comes from the random association of uncorrelated tracks. Its shape is defined by the detector acceptance and the p_T distribution of particles in the event. This part of the background remains smooth in the mass interval comparable to the width of the peaks shown in Figs. 3–6. The correlated part of the combinatorial background comes from partially or incorrectly reconstructed decays of true particles and jets, and may have a faster changing shape. In several analyses the most significant contributions to the correlated background were studied to verify that they do not affect the raw yield extraction procedure. For example, the decay $\eta \rightarrow \gamma\gamma$ produces an $\eta\gamma$ peak at around 0.6 GeV/ c^2 in the invariant mass distribution of $\pi^0\gamma$. Also, the decay of $K_s^0 \rightarrow \pi^+\pi^-$ produces a peak at ~ 1.07 GeV/ c^2 in the K^+K^- invariant mass distribution when two pions are erroneously assigned the kaon mass. In some cases these processes limit the mass range available for the background determination. The mass range used for the determination of the background did not include regions where one could expect the appearance of such peaks.

The raw yields were measured in the following way. First, the invariant mass distributions in different p_T bins were fitted with the BW * G plus background in the mass range of ± 5 combined widths of the BW * G around the nominal mass of the meson. The exact range varied slightly depending on particle species and the p_T bin. The background contribution, estimated by the polynomial part of the fit function, was subtracted from the measured

invariant mass distribution, and the resulting histogram was used to count the raw yield. Bins lying within ± 2.5 combined widths of the BW * G function around the mass peak contributed to the yield. The same procedure was used to calculate the raw yield in the Monte Carlo calculations used for the acceptance evaluation.

The systematic uncertainty of the raw yield extraction is usually the main contributor to the total systematic uncertainty. We evaluated this uncertainty by modifying the analysis procedure. The main goal was to change the shape of the background around the resonance peak in a manner similar to that shown in Fig. 5. To achieve this goal, analyses of the same decay modes were performed in different ways—for example, by requiring PC3 or EMCal hit matching for charged tracks, varying the minimum energy of γ clusters, or modifying the selection criteria for π^0 (η) candidates. Independent of this we also varied the parameters of the fit functions, such as the fit range and the order of the polynomial. Typically, six to ten raw yield values were accumulated for each p_T bin. After fully correcting each of them for the corresponding reconstruction efficiency, the rms of the results was taken as the systematic uncertainty.

C. Invariant mass resolution

The invariant mass resolution of the detector plays an important role in the analyses described in this section. It depends on several factors. Use of the detector tracking system or EMCal makes a large difference. The momentum range of the analyzed particles is less important. The difference between the mass of the particle and its decay products contributes directly to the invariant mass resolution. To demonstrate this we consider the limiting case of a particle decaying into two massless products. In this case, one can approximate the invariant mass resolution with the simple relation $\delta m/m = (1/\sqrt{2})\delta p_T/p_T$. The single particle momentum resolution was discussed in Sec. II. Figure 7 compares this approximation with the widths of the peaks shown in Figs. 2–6. The measured widths are plotted as a function of the mass difference between the particle and its decay products. The two lines in the plot are calculated for two-body decays reconstructed either with the tracking system only or with the EMCal only at a pair p_T of 4 GeV/ c .

As can be seen, the simple approximation describes the measured mass widths for the two-body decays reasonably well. The widths of the e^+e^- decay modes are somewhat narrower due to the use of a lower momentum range. The results for the J/ψ and ψ' , which are not shown in the plot, are also consistent with the trend of the “tracking” line. The $\phi \rightarrow K^+K^-$ represents the case where the assumption of massless products is least valid; nevertheless, the agreement is still reasonable.

The widths of the invariant mass peaks reconstructed with both the EMCal and the tracking systems are

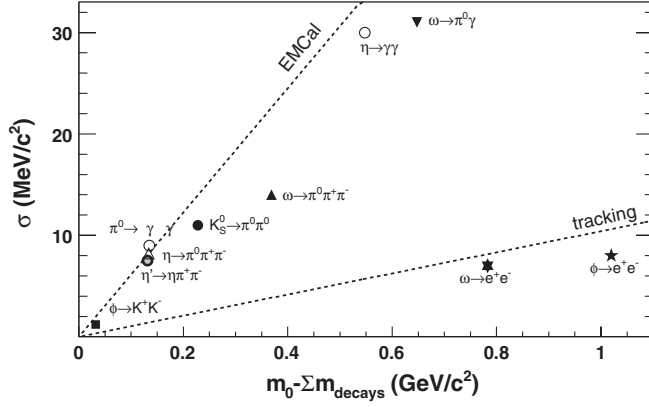


FIG. 7. Invariant mass resolution of the PHENIX detector for different decay modes measured in the momentum range $4 < p_T$ (GeV/c) < 6 , except for the e^+e^- mode that is measured in the range $0.5 < p_T$ (GeV/c) < 0.75 . The lines indicate the expected detector mass resolution.

dominated by the EMCal resolution. However, due to the energy correction applied to the γ clusters forming π^0 or η candidates, the widths of the peaks reconstructed with three and four particles are below the “EMCal” line.

D. Detector acceptance and efficiency

1. Geometrical acceptance and the analysis cuts

The determination of the detector acceptance was done using a single particle Monte Carlo simulation. Particles were uniformly generated within $|y| < 0.5$ in rapidity and in full azimuthal angle. The range of the transverse momentum distributions was chosen to produce sufficient statistics in all p_T bins for which the signal could be extracted from the data. For the acceptance calculation the generated spectra were weighted to match the measured particle spectra. This procedure was done iteratively. Kinematics of the three-body decays of the η , ω , and η' mesons assumed the experimentally measured phase space density distributions [54–59].

The PHENIX detector simulation is based on the GEANT code, which properly reproduces the momentum, spatial, and timing resolution of all detector subsystems and fully describes inactive areas. The simulated positions and widths of the π^0 , K_S^0 , η , ω , η' , and ϕ peaks were consistent with the values measured in real data at all p_T 's. The same analysis code was used for the reconstruction and analysis of the simulated and real data.

The detector acceptance, calculated as the ratio of the number of fully reconstructed particles to the number of generated particles, is shown in Fig. 8. All curves take into account the detector geometry, particle decay kinematics, performance of the detector subsystems including particle identification, and the analysis cuts. The efficiencies strongly depend on the particle momentum and rapidly decrease at low p_T for all species studied in this analysis, establishing a low p_T edge for the measurements.

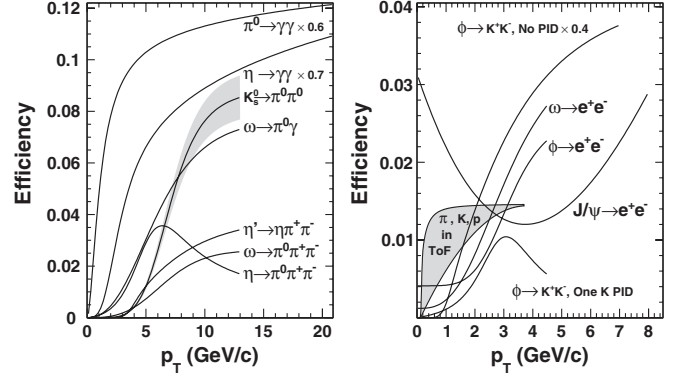


FIG. 8. Detector acceptance as a function of transverse momentum for different particles measured with the PHENIX experiment. The scaling factors allow clear comparison of the p_T dependence of the efficiency of rare and common decay channels. The band in the left panel shows the largest relative systematic uncertainty among all curves.

2. ERT trigger efficiency

The analysis of several decay modes was based on data samples accumulated with the ERT trigger described in Sec. II. The ERT trigger efficiency was extracted using the minimum bias event sample. Each EMCal cluster which set the ERT trigger bit to indicate a γ cluster or electron was identified. The track or cluster had to also satisfy the analysis cuts of a particular decay mode, and match the region where the trigger bit was generated. The trigger efficiency was calculated as the energy spectra of such clusters divided by the energy spectra of all accepted clusters or electrons. Trigger efficiencies of photons and electrons measured for one of the PbSc sectors as a function of cluster energy are shown in the left panel of Fig. 9.

The trigger efficiencies grow steeply with energy, reaching 50% at values approximately corresponding to the online trigger threshold setting of 0.6 GeV for electrons and 1.4 GeV for photons. The curves saturate at approximately twice the threshold energy. The level of saturation is below 100% because of inactive areas of the ERT and the RICH efficiency.

For the analyzed decay modes the trigger efficiency evaluation was done using the same Monte Carlo sample as was used for the acceptance calculation. First we required the particle to be reconstructed in PHENIX without the ERT trigger requirement. Then, for all EMCal clusters associated with photons or electrons in the final state of the decay, we generated a random number between 0 and 1 and compared it to the magnitude of the curve shown in the left panel of Fig. 9 at the energy of the cluster. The particle was considered to fire the ERT trigger if at least one of the randomly generated numbers was lower than the corresponding value of the curve. The probability to fire the ERT trigger for all analyzed mesons is shown in the right panel of the same figure.

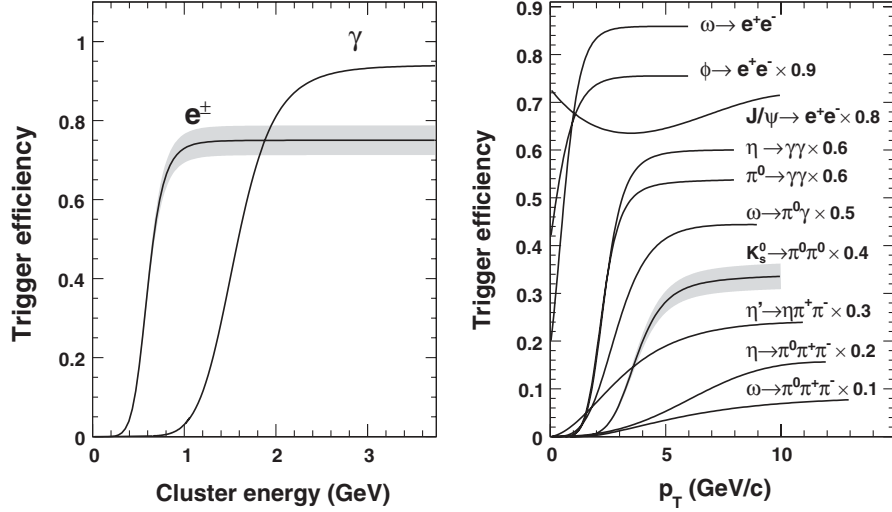


FIG. 9. Efficiencies of the ERT 4×4 and ERT 2×2 triggers for single γ clusters and electrons as a function of energy (left panel). Trigger efficiencies for different meson decays as determined from Monte Carlo simulation (right panel). The band shows the largest relative systematic uncertainty among all curves. The scaling factors are used for visual clarity.

3. Electron identification efficiency

The electron identification efficiency is included in the acceptance efficiencies shown in Fig. 8. It was evaluated using a full detector Monte Carlo simulation which was tuned to adequately reproduce the RICH and the EMCal detector responses. To ensure that the electron identification efficiency was properly done in the simulation, it was confirmed to agree with the efficiency measured with real data.

For this comparison the data samples accumulated during special PHENIX runs were used. In those runs a 1.7%

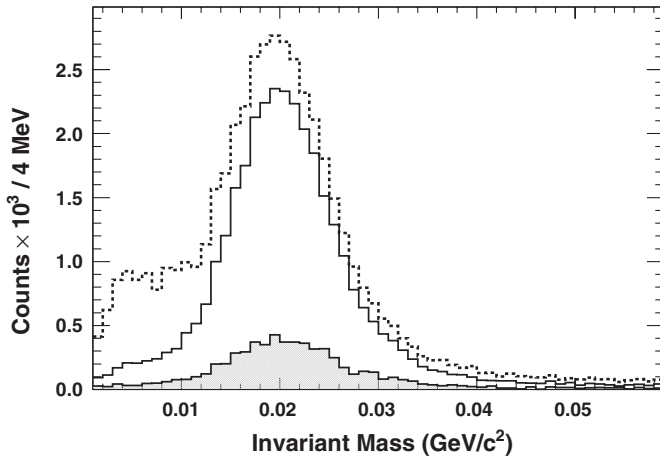


FIG. 10. Invariant mass distribution for e^+e^- pairs, where one track is identified as an electron and the second track is any track (dashed line), the same for pairs which open up in the plane perpendicular to the detector magnetic field (solid line), and among those pairs, the ones in which the second track fails the electron identification cut (filled histogram).

radiation length brass converter was installed around the RHIC beam pipe in the PHENIX interaction region. In this sample we selected electrons of both signs using very strict electron identification requirements. Those electrons were paired with all other tracks in the event. The invariant mass distribution of such pairs is shown by the upper histogram in Fig. 10.

One can see the characteristic shape of the partially reconstructed π^0 Dalitz decays and a peak at around 22 MeV/c² corresponding to γ conversions close to the beam pipe. Since the conversion electrons originate at the displaced converter vertex, and therefore skip the first 3.8 cm of the magnetic field, the reconstructed invariant mass peak is shifted from zero. Among these pairs a further selection was made to choose those which open up in the plane perpendicular to the detector magnetic field. This requirement effectively suppresses the combinatorial background and pairs coming from the π^0 Dalitz decays, but does not suppress $\gamma \rightarrow e^+e^-$ pairs having small opening angles. The middle histogram in Fig. 10 shows that the conversion peak significantly dominates the residual Dalitz contribution and the combinatorial background. Finally, we applied the electron identification requirements to the second track. The invariant mass distribution of the pairs where the second track fails to be identified as an electron is shown by the filled histogram. The ratio of the lowest to the middle histogram under the peak is the electron identification loss. It reaches 20% below 0.5 GeV/c and saturates at $\sim 10\%$.

E. Calculation of invariant cross sections

The invariant cross section for a particle in each p_T bin was calculated as

TABLE I. Relative systematic uncertainties (in percent) for different decay modes. Given ranges indicate the variation of the systematic uncertainty over the p_T range of the measurement.

Particle decay	K_s^0 $\pi^0\pi^0$	$\pi^0\pi^+\pi^-$	ω $\pi^0\gamma$	e^+e^-	η' $\pi^+\pi^-$	ϕ K^+K^-	e^+e^-	Uncertainty type
Acceptance	8	5	6	5	5	5–7	5	B
EMCal energy resolution	4–5	2–5	2–3		2–4			B
EMCal, DC scale	4–6	2–6	3–17	2–11	2–5	1–5	2–10	B
π^0 , η selection	5–10	3	3		3			B
ERT trigger efficiency	2–12	3–10	2–7	1–3	2–4		1–2	B
Peak extraction MC	2	1	1	1	1	3	1	A, B
Raw yield extraction	4–19	5–17	5–12	4–15	6–25	8–25	3–11	A, B
γ conversion	6	3	5		3			C
e identification				10			9	B
Branching ratio	0	1	3	1.7	3	1	1.3	C
MinBias trigger	9.7	9.7	9.7	9.7	9.7	9.7	9.7	C
Total	17–29	13–24	15–26	16–24	14–29	14–28	15–18	

$$\frac{1}{2\pi p_T} \frac{d^2\sigma}{dp_T dy} = \frac{1}{2\pi p_T} \frac{1}{\mathcal{L} \text{BR}} \frac{1}{\varepsilon(p_T)\varepsilon_{\text{BBC}}} \frac{N(\Delta p_T)}{\Delta p_T \Delta y}, \quad (1)$$

where $N(\Delta p_T)$ is the number of reconstructed particles in a given p_T bin, \mathcal{L} is the integrated luminosity sampled by the minimum bias trigger, $\varepsilon(p_T)$ is the acceptance and reconstruction efficiency, BR is the branching ratio, and ε_{BBC} is the minimum bias trigger efficiency for events containing mesons, estimated to be 0.79 ± 0.02 . The cross section sampled by the BBC trigger, $\sigma_{\text{tot}}^{pp} = 23.0 \pm 2.2$ mb, was used to determine the integrated luminosity. For the analyses with the minimum bias data sample, $\varepsilon(p_T)$ corrects for the acceptance and reconstruction efficiency, while for analyses with the ERT data sample, it includes the ERT trigger efficiencies as well. A bin shift correction was applied to take into account the finite width of the p_T bins used in the analyses. The correction is made by shifting the data points along the vertical axis according to the procedure described in [60].

Finally, in the $\omega \rightarrow \pi^0\pi^+\pi^-$ and $K_s^0 \rightarrow \pi^0\pi^0$ analyses, the cross sections measured with the ERT and with the minimum bias triggers were averaged in the overlapping p_T region, taking into account the statistical and systematic uncertainties.

F. Systematic uncertainties

In addition to the systematic uncertainties described in the corresponding analysis sections, uncertainties of the ERT trigger efficiency and acceptance corrections were estimated by varying the analysis cuts, and by varying the energy and momentum scales of the EMCal and DC by 1%. The resulting systematic uncertainties for the different decay modes of K_s^0 , η , ω , η' , and ϕ mesons are summarized in Table I. The uncertainties are categorized by types: (A) uncorrelated between p_T bins, (B) p_T correlated, all points moving in the same direction but not by the same factor, and (C) an overall normalization uncertainty in which all points move by the same factor, independent of p_T . The type C

uncertainty is predominantly due to the uncertainty of the minimum bias trigger efficiency in $p + p$ collisions, equal to 9.7% [1,2]. The uncertainty of the raw yield extraction is estimated as described in Sec. III B. It dominates the total uncertainty and is split into type A and type B contributions.

G. Neutral meson spectra

The invariant differential cross sections calculated using Eq. (1) are tabulated in Tables X and XI in the Appendix and plotted in Fig. 11. Different symbols are used to show results for different decay modes. One can see a very good

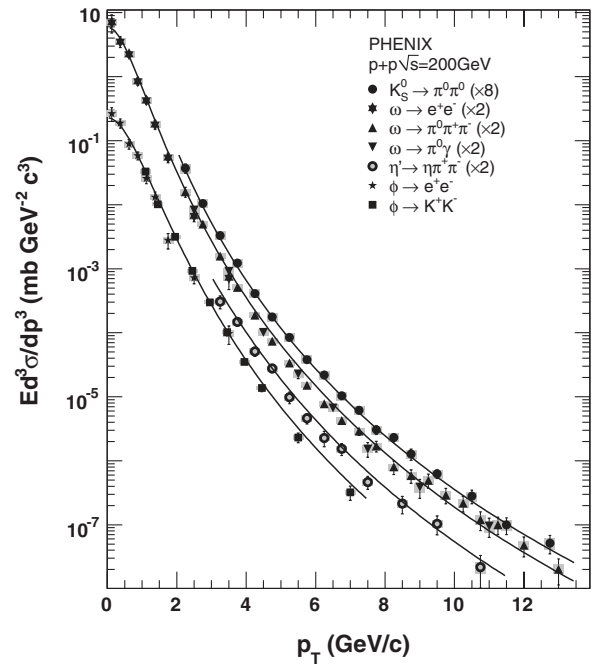


FIG. 11. Invariant differential cross section of neutral mesons measured in $p + p$ collisions at $\sqrt{s} = 200$ GeV in various decay modes. The lines are fits to the spectra as described further in the text.

agreement between the particle spectra measured in the different decay modes. Results for low p_T bins for particles reconstructed through decays in the e^+e^- mode allow an accurate measurement of the integrated particle yield. The integrated yield at midrapidity for the ω is measured to be $d\sigma^\omega/dy = 4.20 \pm 0.33^{\text{stat}} \pm 0.52^{\text{syst}}$ mb, and for the ϕ it is measured to be $d\sigma^\phi/dy = 0.432 \pm 0.031^{\text{stat}} \pm 0.051^{\text{syst}}$ mb. The mean transverse momenta for these particles are $\langle p_T^\omega \rangle = 0.664 \pm 0.037^{\text{stat}} \pm 0.012^{\text{syst}}$ GeV/ c and $\langle p_T^\phi \rangle = 0.752 \pm 0.032^{\text{stat}} \pm 0.014^{\text{syst}}$ GeV/ c .

IV. ANALYSIS OF PARTICLE SPECTRA

In this section we analyze the measured invariant transverse momentum spectra for a variety of hadrons in $p + p$ collisions at $\sqrt{s} = 200$ GeV and search for common features. All measurements are quoted as the invariant differential cross sections at midrapidity averaged over the rapidity interval $|y| \leq 0.35$.

$$E \frac{d^3\sigma}{dp^3} = \sigma_{pp}^{\text{inel}} \times \frac{1}{2\pi p_T} \frac{1}{N_{\text{events}}} \frac{d^2N}{dy dp_T}, \quad (2)$$

where $\sigma_{\text{inel}}^{pp} = 42$ mb.

A. Data samples

The procedures used for the reconstruction of the particle transverse momentum spectra are described above in Sec. III and in other PHENIX publications listed in Table II. Figure 11 shows the new results presented in

TABLE II. Data samples used in the analysis of particle spectra. The X and XI in the Reference column refer to Tables X and XI in the Appendix.

Particle	Mode	Physics run	p_T (m_T) range GeV/ c , GeV/ c^2	Reference
π^0	$\gamma\gamma$	5	0.5–20	[3]
π^+ , π^-	TOF	3	0.3–2.7	[1]
K^+ , K^-	TOF	3	0.4–1.9	[1]
K_S^0	$\pi^0\pi^0$	5	2–13.5	XI
η	$\gamma\gamma$	3	2–12	[2]
η	$\gamma\gamma$	6	2–20	[6]
η	$\pi^0\pi^+\pi^-$	3	2.5–8.5	[2]
ω	e^+e^-	5	0–4	X
ω	$\pi^0\pi^+\pi^-$	5	2–13.5	X
ω	$\pi^0\pi^+\pi^-$	3	2.5–10	[4]
ω	$\pi^0\gamma$	5	2–12	X
ω	$\pi^0\gamma$	3	2–7	[4]
η'	$\eta\pi^+\pi^-$	5	3–11.5	XI
ϕ	e^+e^-	5	0–4	XI
ϕ	K^+K^-	5	1–8	XI
J/ψ	e^+e^-	5	0–9	[5]
J/ψ	e^+e^-	6	0–9	[48]
ψ'	e^+e^-	6	0–7	[61]
p , \bar{p}	TOF	3	0.6–3.7	[1]

this paper, and Fig. 12 shows these results compared with previous PHENIX results. All meson spectra used in this paper are not corrected for feed-down.

Figure 12 demonstrates a very good agreement between the new results and previously published data. The results presented in this paper greatly enhance the p_T range of the previously measured particles and add results for particles that have not been previously analyzed.

For each particle we considered all available measurements of the invariant momentum distributions together with their statistical and systematic uncertainties categorized as types A, B, and C, as explained in Sec. III F.

For the analysis of the shape of the transverse momentum distributions, the data for all particles of the same isospin multiplet were combined into one p_T spectrum to be fitted. All data for positively and negatively charged particles measured in the same analysis and in the same p_T bins were averaged. All data for neutral particles, measured via different decay channels, were added together. The notation π is used to denote a combined spectrum of π^0 and $(\pi^+ + \pi^-)/2$, K is used for a combined spectra of K_S^0 and $(K^+ + K^-)/2$, p denotes $(p + \bar{p})/2$, and so forth. Independent measurements of the same particle performed using different data samples or different decay modes were also added together but not averaged. For data samples where the results were published as dN/dp_T , a conversion was made using Eq. (2).

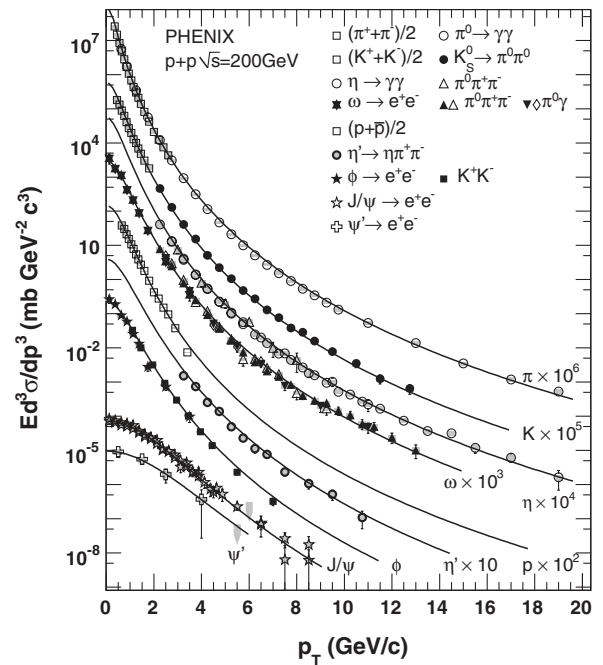


FIG. 12. Invariant differential cross sections of different particles measured in $p + p$ collisions at $\sqrt{s} = 200$ GeV in various decay modes. The spectra published in this paper are shown with closed symbols, and previously published results are shown with open symbols. The curves are the fit results discussed in the text.

B. Particle spectra fit distributions

It is widely known from experimental data that, as expected from pQCD calculations (e.g. [62]), a pure power law shape successfully describes the high- p_T region of particle spectra:

$$E \frac{d^3\sigma}{dp^3} = A p_T^{-\nu}, \quad (3)$$

where the shape is determined by the power ν and A is a normalization constant. However, the power law shape is seen to fail in the region below about $p_T = 3\text{--}5$ GeV/ c , where the spectra exhibit a more exponential shape.

The exponential shape of the particle spectra at low p_T suggests a thermal interpretation in which the bulk of the produced particles is emitted by a system in thermal equilibrium with a Boltzmann-Gibbs statistical description of their spectra:

$$E \frac{d^3\sigma}{dp^3} = C_b e^{-E/T}, \quad (4)$$

where C_b is a normalization factor and E is the particle energy. At midrapidity one can replace E by $m_T = (p_T^2 + m_0^2)^{1/2}$, where m_0 is the particle rest mass.

In recent years a variety of publications [7,26–30,63] have used the Tsallis distribution [24] to fit particle spectra. The Tsallis distribution derives from a generalized form of the Boltzmann-Gibbs entropy and is written as

$$G_q(E) = C_q \left(1 - (1 - q) \frac{E}{T}\right)^{1/(1-q)}, \quad (5)$$

where C_q , E , and T have similar meanings as in Eq. (4) and q is the so-called nonextensivity parameter. For values of $q \neq 1$ the distribution exhibits a power law behavior with power $n = -1/(1 - q)$. In order to associate the Tsallis distribution with a probability distribution, which describes the invariant particle spectra given by Eq. (2) and defined over $0 < E < \infty$, Eq. (5) must satisfy a normalization and energy conservation condition $\langle E \rangle < \infty$. This limits the range of the parameter q to $1 < q < 1\frac{1}{3}$. The Tsallis distribution reduces to the Boltzmann-Gibbs distribution of Eq. (4) in the limit of $q \rightarrow 1$.

To put Eq. (5) into a form appropriate to fit particle spectra, we replace E by $m_T = (p_T^2 + m_0^2)^{1/2}$ and use the requirement of unit normalization to determine the coefficient C_q in Eq. (5) to be equal to

$$C_q = \frac{(2q - 3)(q - 2)}{T(T + m_0) - (q - 1)(q - 2)m_0^2} \times \frac{1}{(1 - (1 - q) \frac{m_0}{T})^{1/(1-q)}}. \quad (6)$$

We replace the parameter q with

$$n = -\frac{1}{1 - q}. \quad (7)$$

The resulting formula used in the fitting procedure is given by

$$E \frac{d^3\sigma}{dp^3} = \frac{1}{2\pi} \frac{d\sigma}{dy} \frac{(n - 1)(n - 2)}{(nT + m_0(n - 1))(nT + m_0)} \left(\frac{nT + m_T}{nT + m_0}\right)^{-n}, \quad (8)$$

where $d\sigma/dy$ is the integrated cross section of the particle production at midrapidity.

In the limit of $m_0 \rightarrow 0$ Eq. (8) becomes

$$E \frac{d^3\sigma}{dp^3} = \frac{1}{2\pi} \frac{d\sigma}{dy} \frac{(n - 1)(n - 2)}{(nT)^2} \left(1 + \frac{m_T}{nT}\right)^{-n}. \quad (9)$$

This form is very similar to the QCD inspired expression suggested by Hagedorn in [22] written as a function of m_T instead of p_T .

The condition that the shapes of the m_T spectra of different particles are the same regardless of their mass is referred to as m_T scaling. m_T scaling is known to provide a good description of the experimental data at low energy, where the spectral shapes are exponential [18,23]. Because of the explicit m_0 mass dependence in Eq. (8) the Tsallis distribution does not satisfy m_T scaling, except in the case $m_0 \rightarrow 0$ or $q \rightarrow 1$, in which case the limiting forms of Eq. (4) or (9) apply. Therefore, the accuracy of fits to the Tsallis distribution and the validity of m_T scaling need to be quantified with data.

The power law behavior at high p_T which appears in Eq. (8) is governed by the parameter n . The parameter n can be related to the simple power law parameter ν that occurs in Eq. (3) through the condition that both expressions have the same power-law slope at a given p_T . From Eqs. (3) and (8) one can write

$$\frac{d \ln(nT + m_T)^{-n}}{d \ln(p_T)} = \frac{d \ln(p_T^{-\nu})}{d \ln(p_T)}, \quad n = \frac{\nu m_T^2}{p_T^2 - \nu T m_T}. \quad (10)$$

At high p_T ($p_T \gg m_0, \nu T$), where one can neglect the difference between m_T and p_T , ν and n coincide. In the p_T region where most particle spectra are measured, n is 15%–25% larger than ν .

The mean m_T of the Tsallis distribution in the form of Eq. (8) is calculated as

$$\begin{aligned} \langle m_T \rangle &= \frac{2nT}{n - 3} + \frac{(n - 2)(n - 1)}{(nT + m_0(n - 1))(n - 3)} m_0^2 \\ &\approx \frac{2nT}{n - 3} + \frac{n - 2}{n - 3} m_0. \end{aligned} \quad (11)$$

The approximate relation requires $m_0 \gg T$. This condition is satisfied for all particles, except pions, for which T and m_0 are about the same. Similarly, the mean p_T can be well approximated for all measured particles with a linear dependence:

$$\langle p_T \rangle \approx \frac{2nT}{n-3} + f(n)m_0. \quad (12)$$

The first contribution is identical to that in Eq. (11), and $f(n)$ has only a weak dependence on m_0 , which we neglect in Eq. (12).

The Tsallis distribution is appealing to use to describe particle spectra because it provides a single functional form that can reproduce the full spectral shape with just two parameters. Tsallis distributions have been used successfully to describe particle spectra in different collision systems and at different energies [7,26–30,64–66]. Tsallis distributions also describe various physics phenomena beyond particle production and have been successfully applied in other fields of science; see [64,67–69] and references therein.

As mentioned above, the Tsallis distribution was derived as the single particle distribution corresponding to a generalization of the Boltzmann-Gibbs entropy through the introduction of the nonextensivity parameter q [24]. Whereas the Boltzmann-Gibbs distributions are found to apply to systems which exhibit an exponential relaxation in time to a stationary state characterized by exponentials in energy at thermal equilibrium, the generalized form is found to apply to systems which exhibit power laws in relaxation time and energy. These are systems which relax with a nonergodic occupation of phase space as a consequence of the microscopic dynamics of the system. Among other examples, this is characteristic of systems with long-range interactions that fall off with distance with a power smaller than the dimensionality of the system. It is an interesting question whether strongly interacting partonic matter might also exhibit power law relaxation. In fact, an analysis of the diffusion of a charmed quark in partonic matter produced in parton cascade calculations found that the parton densities were characterized by Tsallis distributions, rather than Boltzmann-Gibbs distributions [70].

The physical interpretation of the parameter T in Eq. (5), especially in $p + p$ collisions, is not straightforward. One can expect that for larger systems, such as those produced in relativistic heavy ion collisions, T reflects the kinetic freeze-out temperature $\langle T_{\text{kfo}} \rangle$ at which particle scattering ceases to modify the spectral shapes. It is shown below that the magnitudes of $\langle T \rangle$ found in this work are close to $\langle T_{\text{kfo}} \rangle$ extracted in the blast-wave model approach [8,71] applied to $p + p$ data. In applications to $p + p$ collisions it has been shown [25] that the parameter q of the Tsallis distribution of Eq. (5) can be related to the amount of temperature fluctuations in the system as

$$q = 1 + \frac{\text{Var}(\frac{1}{T})}{\langle \frac{1}{T} \rangle^2} = 1 + \frac{1}{n}. \quad (13)$$

C. Fitting procedure

In order to obtain a reliable estimate of the fit uncertainties, the experimental systematic uncertainties must be

treated properly. The various types of systematic uncertainties have been taken into consideration as described here. The p_T -independent systematic uncertainties of type A have been combined in quadrature with the statistical errors, and the p_T -independent systematic uncertainties of type C were reduced by 9.7% due to the trigger uncertainty, common to all analyzed particles. Residual uncertainties of type C and of type B must also be considered in the analysis. The type B uncertainties, by definition, have an unknown p_T dependence. In order to estimate their effect, the particle spectra were varied and fit multiple times. For each fit the y coordinate in each p_T bin was varied by the same amount according to the uncertainty of type C, and by differing amounts according to the type B uncertainties, in a manner similar to that explained in [72].

Variations of the y coordinates were made independently for each fit with the amount of variation chosen randomly according to the p_T -dependent uncertainties for each particle and each sample. For the particle spectra consisting of multiple samples, results of each fit to the entire spectrum were weighted with the probability of the fit estimated from the χ^2 criteria. Such weighting emphasizes variations in which individual samples fluctuate toward each other rather than away from each other, which corresponds to the assumption that the different samples represent measurements of the same true momentum distribution.

As a result of the multiple fits, weighted distributions of the fit parameters were obtained. The mean of the distribution was taken as the parameter value, the rms width of the distribution was taken as the systematic uncertainty, and the statistical uncertainty was taken from the fit to the unmodified data. The number of fits was chosen such that the mean and the rms did not change with an increasing number of trials.

D. Fit results

The fits of Eq. (8) to the data are shown in Fig. 13 with dotted lines. The results are given in Table III.

The fit parameters n and T are strongly correlated. The magnitude of the correlation coefficient between these two parameters for all species listed in Table III exceeds 0.9. Therefore, additional information is needed to constrain the values of n and T . For that purpose one can use a power law given by Eq. (3) fitted to the same data. As discussed above, the parameters n and ν are related to each other through Eq. (10). However, it is found that the results of the power law fit depend on the fit range, but become stable when the fit range begins above $p_T \sim 3.5$ GeV/ c for most particles, or above $p_T \sim 5.5$ GeV/ c for heavier particles such as the J/ψ . The resulting power law fits are shown in Fig. 13 as dashed lines that have been plotted down to $p_T = 0.5$ GeV/ c . Spectra without sufficient data above the fit range lower limit were not fitted. The results are given in Table IV.

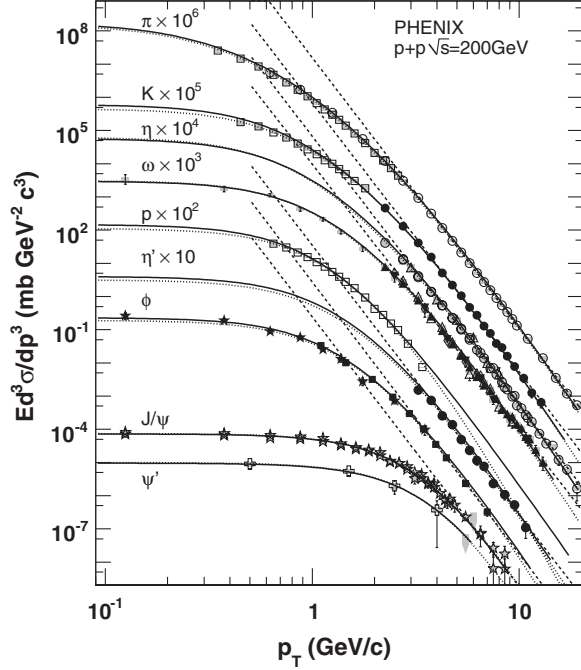


FIG. 13. The p_T spectra of various hadrons measured by PHENIX fitted to the power law fit (dashed lines) and Tsallis fit (solid lines). See text for more details.

The parameters ν of the power law fits and the parameters n and T of the Tsallis fits are shown in Fig. 14 as a function of the particle mass. The parameters have been fit to a linear function to establish if there is a mass dependence. The fits are shown in Fig. 14 as solid lines, with the uncertainties indicated by dashed lines. From Fig. 14 it is evident that the parameters are consistent, with no significant mass dependence. Therefore, the parameters have also been fit with a constant value. The results for the linear and constant fits are summarized in Table V.

The fitted linear coefficients are consistent with zero mass dependence within less than 2 standard deviations of the fit accuracy for all three parameters. At the same time, the parameter ν is more accurately defined compared

TABLE IV. Parameters of the power law fit with Eq. (3). The uncertainties are statistical and systematic. Units of A are $\text{mb} (\text{GeV}/c)^{\nu+2}$.

	ν	A
π	$8.174 \pm 0.035 \pm 0.049$	$16.4 \pm 1.1 \pm 1.6$
K	$8.24 \pm 0.08 \pm 0.11$	$8.8 \pm 0.9 \pm 1.6$
η	$8.169 \pm 0.037 \pm 0.054$	$7.64 \pm 0.46 \pm 0.83$
ω	$7.986 \pm 0.083 \pm 0.080$	$9.5 \pm 1.3 \pm 1.4$
η'	$8.12 \pm 0.21 \pm 0.11$	$3.6 \pm 1.2 \pm 0.8$
ϕ	$8.20 \pm 0.36 \pm 0.15$	$2.8 \pm 1.5 \pm 0.7$
J/ψ	$7.0 \pm 1.2 \pm 0.4$	$0.03 \pm 0.03 \pm 0.02$

to the Tsallis fit parameter n . We can invoke Eq. (10) to constrain the Tsallis fit using the parameter ν . This requires estimating the effective p_T which appears in Eq. (10). Using the mass-independent terms of the fits listed in Table V, the effective p_T is about $7 \text{ GeV}/c$.

This value is large enough to allow one to neglect the difference between m_T and p_T in Eq. (10) for all particles, except the J/ψ and ψ' . These two particles do not constrain the mass dependence of the Tsallis fit parameters due to their large fit uncertainties, as shown in Fig. 14.

Under the assumption that the parameter ν is the same for all particles, the mass dependence of the parameters n and T must either be present or absent together. This can be checked by fixing the parameter n to a constant value of $n = 9.656$ (from Table V) and fitting the data again. The mass-dependent coefficient for the parameter T that results in this case is somewhat different from zero, compared to uncertainties. This is a clear contradiction to Eq. (10) under the assumption of constant ν , and therefore indicates that the parameters n and T have a mass dependence. However, this conclusion is at the limit of the accuracy of the currently available data.

For further analysis the parameter n was fixed to have a linear dependence $n = 9.48 + 0.66m_0 [\text{GeV}/c^2]$ (from Table V), and the particle spectra were fit again. The results are given in Table VI, and the fit to the mass dependence of T is given in Table VII.

TABLE III. Parameters of the Tsallis fit with Eq. (8) with all parameters free to vary. The uncertainties are statistical and systematic. Cross sections are in μb for J/ψ and ψ' , and in mb for all other particles.

	$d\sigma/dy$ (mb, μb)	T (MeV)	$n = -1/(1 - q)$
π	$43.5 \pm 2.0 \pm 1.9$	$112.7 \pm 2.9 \pm 1.1$	$9.57 \pm 0.11 \pm 0.03$
K	$4.0 \pm 0.1 \pm 0.5$	$132.7 \pm 3.8 \pm 7.2$	$10.04 \pm 0.16 \pm 0.27$
η	$5.1 \pm 1.1 \pm 3.9$	$119 \pm 10 \pm 30$	$9.68 \pm 0.18 \pm 0.49$
ω	$4.3 \pm 0.3 \pm 0.4$	$109.7 \pm 6.9 \pm 6.7$	$9.78 \pm 0.24 \pm 0.18$
η'	$0.80 \pm 1.5 \pm 0.7$	$141 \pm 107 \pm 61$	$10.5 \pm 2.2 \pm 1.2$
ϕ	$0.41 \pm 0.02 \pm 0.03$	$139 \pm 16 \pm 15$	$10.82 \pm 0.71 \pm 0.56$
J/ψ	$0.73 \pm 0.01 \pm 0.05$	$149 \pm 56 \pm 82$	$12.3 \pm 1.6 \pm 2.9$
ψ'	$0.13 \pm 0.03 \pm 0.02$	$164 \pm 10^3 \pm 10^2$	$14 \pm 12 \pm 6$
p	$1.63 \pm 0.05 \pm 0.11$	$107 \pm 13 \pm 12$	$12.2 \pm 1.0 \pm 0.7$

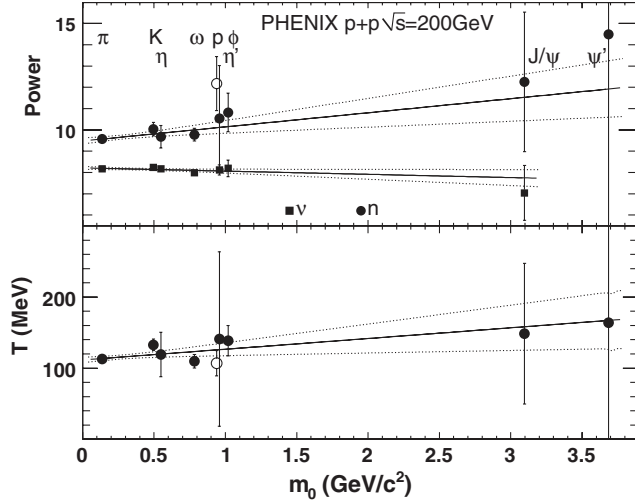


FIG. 14. Particle mass dependence of the fit parameters. Power law parameters ν and n are plotted in the upper panel. Vertical bars denote the combined statistical and systematic uncertainties. The solid lines are linear fits. The dashed lines denote the uncertainty within which the linear fit can be inclined. The lower panel shows the same for the fit parameter T . The proton measurement (open circle) is not used in the fits.

TABLE VII. Constant and linear fits to the Tsallis parameter T of mesons with the fixed parameter n . The last column gives the probability estimated by the $\chi^2/\text{n.d.f.}$ of the fit.

	Fit	Probability
T (MeV)	117.4 ± 2.5	0.64
T (MeV)	$(112.6 \pm 3.8) + (11.8 \pm 7.0)m_0$ (GeV/ c^2)	0.83

Comparison of the results listed in Tables III and VI reveals that the parameters of the fit did not change significantly within uncertainties, even for the η and η' mesons which are not measured at low p_T . In addition, with the n parameter constrained, the uncertainty on the parameter T is reduced.

Since there is not yet a published PHENIX measurement of protons at high p_T , the parameter ν cannot be determined for the case of protons. Results published in [7] suggest that the slope of the proton spectra at high p_T is the same as that for mesons. Using this assumption allows us to extract the parameter T for protons, with the results listed in Table VI. The value of T for protons differs from the values extracted for mesons.

TABLE V. Constant and linear fits to the power law and Tsallis fit parameters. The last column gives the probability estimated by the $\chi^2/\text{n.d.f.}$ of the fit.

	Fit	Probability
ν	8.154 ± 0.039	0.75
ν	$(8.22 \pm 0.07) - (0.15 \pm 0.14)m_0$ (GeV/ c^2)	0.79
n	9.656 ± 0.097	0.69
n	$(9.48 \pm 0.14) + (0.66 \pm 0.39)m_0$ (GeV/ c^2)	0.94
T (MeV)	115.3 ± 2.8	0.43
T (MeV)	$(111.5 \pm 4.0) + (15 \pm 12)m_0$ (GeV/ c^2)	0.51

TABLE VI. Parameters of the Tsallis fit with Eq. (8), with the parameter n constrained to a fixed linear dependence on mass (for mesons). The uncertainties for $d\sigma/dy$ and T are statistical and systematic, and are only systematic for n . Cross sections are in μb for J/ψ and ψ' , and in mb for all other particles.

	$d\sigma/dy$ (mb, μb)	T (MeV)	$n = -1/(1 - q)$
π	$42.8 \pm 3.1 \pm 2.7$	$112.6 \pm 2.1 \pm 2.8$	9.57 ± 0.10
K	$4.23 \pm 0.09 \pm 0.53$	$125.4 \pm 0.9 \pm 5.3$	9.81 ± 0.13
η	$3.86 \pm 0.30 \pm 0.71$	$124 \pm 2 \pm 12$	9.84 ± 0.14
ω	$4.26 \pm 0.23 \pm 0.33$	$115.5 \pm 2.1 \pm 6.8$	10.00 ± 0.22
η'	$0.63 \pm 0.27 \pm 0.21$	$123 \pm 17 \pm 18$	10.12 ± 0.28
ϕ	$0.427 \pm 0.019 \pm 0.023$	$123.4 \pm 3.0 \pm 8.3$	10.16 ± 0.31
J/ψ	$0.760 \pm 0.014 \pm 0.048$	$148 \pm 8 \pm 35$	11.5 ± 1.1
ψ'	$0.132 \pm 0.029 \pm 0.020$	$147 \pm 127 \pm 54$	11.9 ± 1.3
p	$1.775 \pm 0.044 \pm 0.066$	$58.8 \pm 1.8 \pm 6.1$	9.20 ± 0.28

TABLE VIII. Parameters of the Tsallis fit with Eq. (8), with the parameters n and T constrained to have a fixed linear dependence on mass (for mesons). The uncertainties for $d\sigma/dy$ are statistical and systematic, and are only systematic for T and n . Cross sections are in μb for J/ψ and ψ' , and in mb for all other particles.

	$d\sigma/dy$ (mb, μb)	T (MeV)	$n = -1/(1 - q)$
π	$40.5 \pm 0.3 \pm 5.8$	114.2 ± 4.0	9.57 ± 0.10
K	$4.71 \pm 0.06 \pm 0.48$	118.4 ± 5.2	9.81 ± 0.13
η	$4.46 \pm 0.05 \pm 0.97$	119.0 ± 5.4	9.84 ± 0.14
ω	$3.64 \pm 0.07 \pm 0.77$	121.8 ± 6.7	10.00 ± 0.22
η'	$0.62 \pm 0.04 \pm 0.16$	123.8 ± 7.7	10.11 ± 0.28
ϕ	$0.421 \pm 0.009 \pm 0.054$	124.5 ± 8.1	10.15 ± 0.31
J/ψ	$0.761 \pm 0.013 \pm 0.060$	149 ± 22	11.5 ± 1.1
ψ'	$0.133 \pm 0.024 \pm 0.019$	156 ± 26	11.9 ± 1.3
p	$1.76 \pm 0.03 \pm 0.16$	58.8 ± 6.4	9.20 ± 0.28

Using the linear dependence of the T parameter, $T = 112.6 + 11.8m_0$ (GeV/c^2), extracted from the fits to the Tsallis distribution with fixed linear dependence of the n parameter (from Table VI), the spectra can be fit once again to obtain an improved normalization parameter. The resulting fits are shown in Fig. 13 as the solid lines, and the results of the fit are given in Table VIII.

The parameters n and T , and their errors, are fixed to the values obtained from the fitted linear dependence of the parameters on particle mass, obtained from the fits of Tables V and VII. The systematic error on the integrated yields reflects the variation of the n and T parameters within the errors. It also includes the uncertainty from the variation of the spectral shapes within errors of types B and C, as explained above.

The fits accurately describe the data. To demonstrate the quality of the fits, the data points have been divided by the fit value, and the ratios are plotted in Fig. 15.

Grey error bars show the combined systematic uncertainty of types B and C, with the type B uncertainties dominating. The dashed lines show the fit uncertainty corridor. The rms of the vertical spread of all points plotted in Fig. 15 is 0.17. If each point is normalized to the combined statistical and systematic error of the data point, the rms of the same distribution is much larger, with a value of 0.88, which indicates that the agreement between the data and the fit is well within errors.

V. DISCUSSION

A. Tsallis fit parameters

The analysis of Sec. IV demonstrated the ability of the Tsallis distribution functional form to fit the full transverse momenta spectra for all different species produced in $p + p$ collisions at $\sqrt{s} = 200$ GeV with only two parameters, $n = -1/(1 - q)$ and T . Furthermore, the values of the two parameters extracted from the fits are approximately the same for all measured mesons.

On the other hand, the observation that the pure power law fit of Eq. (3) to the spectra in the region of $p_T > 3.5$ GeV/c yields the same power $\nu = 8.154 \pm 0.039$ for all particles with higher accuracy than the Tsallis fit indicates that a weak mass dependence of the Tsallis parameters is to be expected. Assuming a weak mass dependence, one gets $T = 112.6 \pm 3.8 + (11.8 \pm 7.0)m_0$ [GeV/c^2] MeV and $n = 9.48 \pm 0.14 + (0.66 \pm 0.39)m_0$ [GeV/c^2], which improves the description of the meson spectra with the Tsallis distribution.

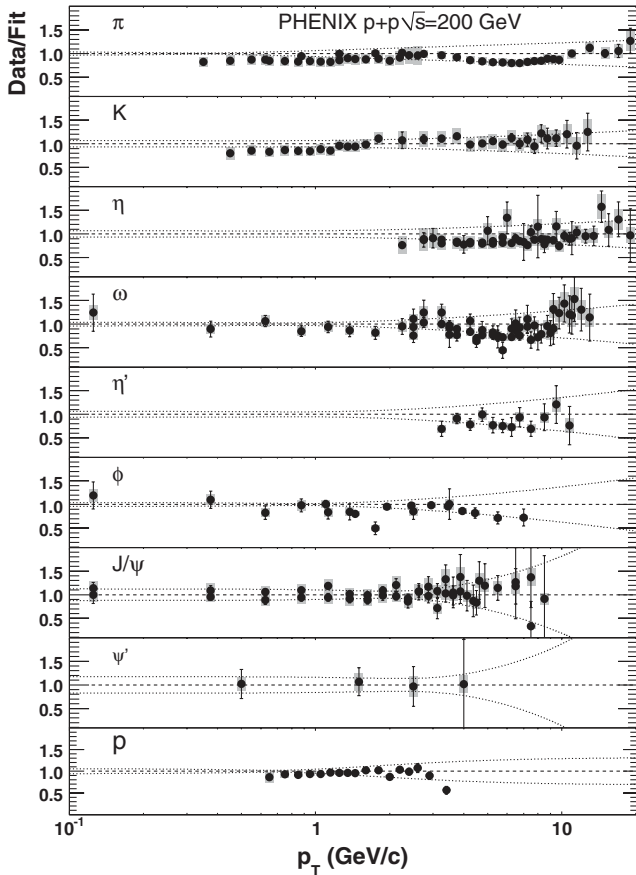


FIG. 15. Data-to-fit ratio for different particles used in the analysis. The systematic uncertainties are the combined uncertainties of type B and type C, excluding the common 9.7% trigger uncertainty.

The parameters are listed in Tables IV and VIII and plotted in Fig. 14.

The ratios of the data points to the Tsallis parametrization using the global fit parameters n and T for all particles were shown in Fig. 15. Represented are nine different particle species measured over the range $0 < p_T$ (GeV/c) < 20 using six independent data samples and ten different analysis techniques. The parametrization is in good agreement with the experimental data. The average deviation of the points from 1 in all panels of Fig. 15 is 88% of the combined uncertainty of the data and the fit.

The Tsallis distribution fit for the proton measurement yields a parameter $T = 58.8 \pm 6.4$ MeV, significantly lower than that for the mesons. Since the published PHENIX results for protons have a limited p_T range, this result was checked and confirmed using STAR measurements for protons and heavier baryons [7–11]. This result indicates significantly different Tsallis fit parameters between mesons and baryons.

The similarity of the measured parameters T and n for all studied mesons suggests a similar production mechanism in $p + p$ collisions at $\sqrt{s} = 200$ GeV. At the same time, the mechanism of baryon production must have different features. The interpretation of the T parameter of the Tsallis fits is not straightforward. If interpreted as a temperature, the values obtained are seen to be similar to average freeze-out temperatures $\langle T_{\text{kfo}} \rangle$ extracted in the blast-wave model approach [8,71] applied to $p + p$ data. As mentioned above, the parameter n can be related to temperature fluctuations as $\sqrt{\text{Var}(1/T)}/\langle 1/T \rangle = 1/n$ in a thermal interpretation. Following this interpretation, one can estimate the fluctuations of the inverse slope parameter $1/T$ to be of order of 0.3.

B. m_T scaling

As discussed in Sec. IV B, m_T scaling can not be an exact scaling when particle spectra follow the Tsallis distribution with $q \neq 1$. However, m_T scaling could be approximately true. The validity of m_T scaling can be studied quantitatively with the assistance of Eq. (9), which gives the Tsallis distribution in the limit $m_0 \rightarrow 0$ with a form explicitly satisfying m_T scaling.

Figure 16 shows the spectra for all particles plotted as a function of m_T and normalized at one single point on the x axis. All normalized spectra are then fit simultaneously with Eq. (9) using fixed parameters taken from Tables V and VII: $n = 9.656$ and $T = 115.3$ MeV for mesons, and $T = 58.8$ MeV for baryons.

The difference in the spectral shapes between mesons and baryons shown in Fig. 16 is due to the large difference in $\langle T \rangle$ between these particle groups. At the same time, the spectra of both mesons and baryons separately are well described by the m_T scaling assumption.

To quantify this statement we restricted the analysis to the PHENIX meson measurements only. After optimization of the normalization point for the different

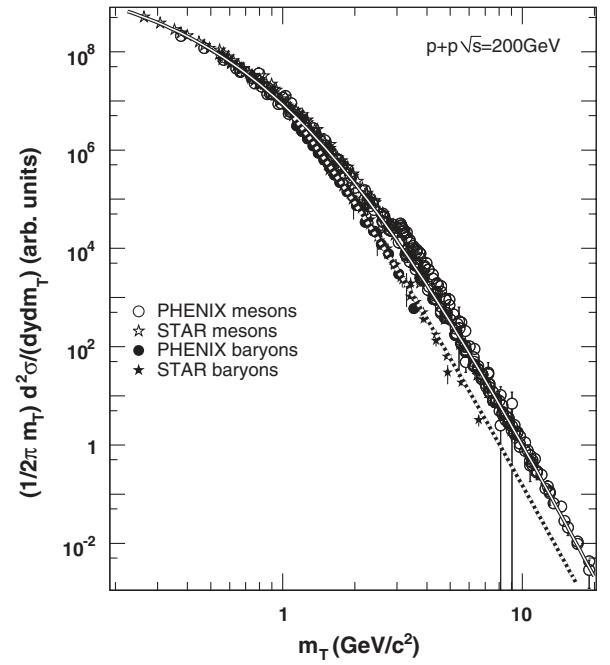


FIG. 16. Particle spectra plotted vs m_T and arbitrarily normalized at $p_T = 10$ GeV/c. Open symbols are mesons and full symbols are baryons measured by PHENIX (circles) and STAR (stars). The lines are the Hagedorn fits by Eq. (9) to mesons (solid) and baryons (dashed) with parameters n and T fixed to average values. Error bars are statistical and point-by-point systematic only.

particles, the rms of the data-to-fit ratio for all points shown in Fig. 16 has a value of 0.25. This is to be compared to the analogous result of Fig. 15 for the Tsallis fit in the p_T coordinate which gave a rms of 0.17. This small increase supports the conclusion that at $\sqrt{s} = 200$ GeV all meson spectra have very similar shapes when plotted as a function of m_T , and thus obey m_T scaling.

C. Integrated yields and $\langle p_T \rangle$

Using the Tsallis functional form and Tables V and VII, one can derive information about $\langle m_T \rangle$ and $\langle p_T \rangle$, based only on the particle mass and the baryon number. Determination of the integrated $d\sigma/dy$ requires experimental measurement of the particle production cross section in at least a limited p_T range.

The results presented below were obtained independently for each particle species without averaging within the same isospin multiplet, unless such averaging was done by the experiment. Different measurements of the same particle were combined together. Published data from the STAR experiment and the references listed in Table IX were also analyzed. To compare PHENIX and STAR results, the spectra and the integrated yields published by STAR, in units of dN/dy, were multiplied by 30 mb, which is the value of the STAR minimum bias cross section in

TABLE IX. Cross sections in mb and $\langle p_T \rangle$ in GeV/ c of different particles in $p + p$ collisions at $\sqrt{s} = 200$ GeV. The PHENIX and STAR columns show the values obtained by fits to the experimental spectra with the Tsallis functional form as described in the text. One should state explicitly that these values do not supersede values given in the “Published” column by the experiments, in their publications listed in the last column, or elsewhere. An additional 9.7% systematic uncertainty should be added to all $d\sigma/dy$ values listed in the column “PHENIX” and 12% to the values in the column “STAR” to account for the trigger uncertainties. Values in the column Published are also given without these systematic uncertainties. The column “SM” is the prediction of the statistical model discussed in the text. The characteristic widths of the particle spectra are $\langle p_T \rangle$ for all species except for J/ψ and ψ' , for which the values given in the table are $\langle p_T^2 \rangle$. For ψ' the integration is done in the p_T region below 5 GeV/ c . All errors are the combined statistical and systematic uncertainties.

Particle	$d\sigma/dy$ (mb)				$\langle p_T \rangle$ (GeV/ c), $\langle p_T^2 \rangle$ (GeV ² / c^2)		Reference
	PHENIX	STAR	Published	SM	Fit	Published	
π^0	41.4 ± 5.8			46.9	0.377 ± 0.012		
π^+	39.4 ± 7.3	43.8 ± 3.3	43.2 ± 3.3	42.1	0.379 ± 0.012	0.348 ± 0.018	[8]
π^-	38.6 ± 7.2	43.2 ± 3.3	42.6 ± 3.3	41.5	0.379 ± 0.012	0.348 ± 0.018	[8]
K^+	4.57 ± 0.61	4.72 ± 0.39	4.50 ± 0.39	4.57	0.567 ± 0.017	0.517 ± 0.030	[8]
K^-	4.20 ± 0.51	4.61 ± 0.18	4.35 ± 0.39	4.38	0.567 ± 0.017	0.517 ± 0.030	[8]
K_S^0	5.28 ± 0.53	4.26 ± 0.15	4.02 ± 0.34	4.40	0.569 ± 0.017	0.605 ± 0.025	[9]
η	4.47 ± 0.96			4.93	0.595 ± 0.018		
ρ		6.55 ± 0.37	7.8 ± 1.2	5.58	0.714 ± 0.019	0.616 ± 0.062	[73]
ω	3.65 ± 0.77		4.20 ± 0.47	5.03	0.718 ± 0.022	0.664 ± 0.039	This work
η'	0.62 ± 0.17			0.365	0.808 ± 0.026		
$(K^{*+} + K^{*-})/2$		1.46 ± 0.10		1.57	0.774 ± 0.022		
$(K^{*0} + \bar{K}^{*0})/2$		1.525 ± 0.091	1.52 ± 0.19	1.55	0.776 ± 0.022	0.81 ± 0.14	[63]
ϕ	0.421 ± 0.055		0.432 ± 0.035	0.339	0.839 ± 0.027	0.752 ± 0.043	This work
ϕ		0.525 ± 0.018	0.540 ± 0.086	0.339	0.839 ± 0.025	0.820 ± 0.051	[74]
$J/\psi (\times 10^3)$	0.759 ± 0.053		0.746 ± 0.089		4.464 ± 0.606	4.60 ± 0.19	[5]
$\psi' (\times 10^3)$	0.133 ± 0.031		0.126 ± 0.034		4.807 ± 0.443	4.7 ± 1.3	[61]
p		4.06 ± 0.23	4.14 ± 0.30	4.47	0.648 ± 0.019	0.661 ± 0.022	[8]
\bar{p}		3.28 ± 0.23	3.39 ± 0.36	3.59	0.648 ± 0.019	0.661 ± 0.022	[8]
Λ		1.33 ± 0.13	1.31 ± 0.12	1.30	0.742 ± 0.023	0.775 ± 0.040	[9]
$\bar{\Lambda}$		1.20 ± 0.12	1.19 ± 0.11	1.11	0.742 ± 0.023	0.763 ± 0.040	[9]
Ξ^-		0.094 ± 0.020	0.078 ± 0.028	0.092	0.850 ± 0.030	0.924 ± 0.054	[9]
Ξ^+		0.091 ± 0.019	0.087 ± 0.031	0.082	0.850 ± 0.030	0.881 ± 0.051	[9]
$\Sigma^{*+} + \Sigma^{*-}$		0.358 ± 0.026	0.321 ± 0.044	0.308	0.882 ± 0.032	1.020 ± 0.073	[10]
$\bar{\Sigma}^{*+} + \bar{\Sigma}^{*-}$		0.310 ± 0.025	0.267 ± 0.038	0.260	0.882 ± 0.032	1.010 ± 0.061	[10]
$\bar{\Lambda}^* + \Lambda^*$		0.127 ± 0.013	0.104 ± 0.017	0.168	0.955 ± 0.038	1.08 ± 0.10	[10]
$\Omega^- + \bar{\Omega}^+ (\times 10^3)$		11.5 ± 4.6	10.2 ± 5.7	17.1	1.035 ± 0.046	1.08 ± 0.30	[9]

$p + p$ collisions at $\sqrt{s} = 200$ GeV, including the nonsingle diffractive part of $p + p$ interactions (cf. [8]).

The particle spectra published by the STAR experiment were fit to the Tsallis functional form given by Eq. (8) with the parameters $n = 9.48 + 0.66m_0$ [GeV/ c^2] and $T = 112.6 + 11.8m_0$ [GeV/ c^2] taken from the global fit to the PHENIX data. The same parameters determined independently for the STAR data give consistent results for mesons. For baryons the STAR data showed a dependence of the parameter T on the mass of the particle; however, the fit uncertainties were too large to make a definite statement. The value of T averaged over all baryon measurements made by STAR agrees with the PHENIX result for the proton measurement. Calculation of $d\sigma/dy$ for p and \bar{p} measured by PHENIX was not done because the spectra are feed-down corrected and the extrapolation to low

p_T requires additional evaluation of the systematic uncertainties.

Figure 17 shows a comparison of the experimentally measured integrated spectral characteristics to the results obtained using the Tsallis fits. The ratio of the measured characteristic width to the width calculated from the Tsallis fit is shown in the upper panel. For most particles the width is taken to be $\langle p_T \rangle$, but for the J/ψ and ψ' the comparison is done for $\langle p_T^2 \rangle$ because this is the parameter published in the corresponding articles. Statistical and systematic uncertainties of the published results are shown at each data point, and the uncertainties of the Tsallis fit values are shown by the band around $y = 1$.

For all mesons the agreement between the published values and the values from the Tsallis fit analysis is consistent with the published uncertainties. This demonstrates

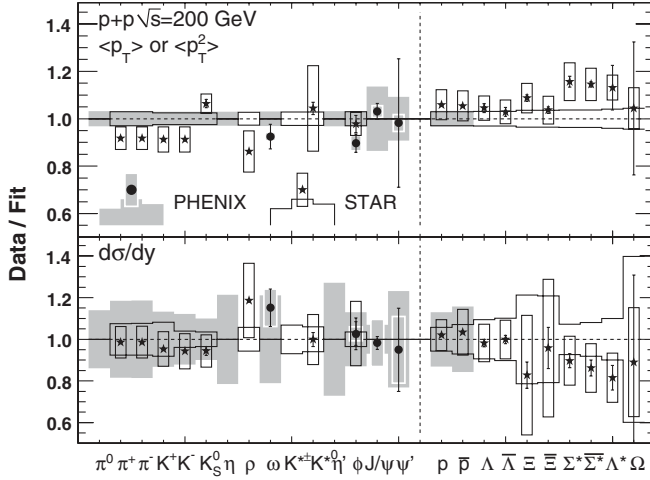


FIG. 17. Comparison of the integrated parameters of the particle spectra. The upper panel shows the ratio of the published result divided by the result of the constrained Tsallis fit for $\langle p_T \rangle$ ($\langle p_T^2 \rangle$) for the J/ψ and the same for ψ' integrated in the p_T range below 5 GeV/c. The lower panel shows the ratio for $d\sigma/dy$. The statistical and systematic uncertainties shown at each point are from the published data only. The band around $y = 1$ shows the uncertainty of the values extracted from the Tsallis function. The trigger efficiency scale uncertainties of 9.7% for PHENIX and 12% for STAR are not plotted. There are no points outside the plot boundaries. The vertical dashed line separates mesons and baryons.

the accuracy to which the Tsallis functional form describes the experimental spectral shapes.

Equation (12) suggests that the mass dependence of the $\langle p_T \rangle$ should be approximately linear. A fit to the average mean momentum of all mesons extracted from the Tsallis distribution fits as a function of their mass gives $\langle p_T \rangle = (0.319 \pm 0.007) [\text{GeV}/c] + (0.491 \pm 0.009)m_0$. A fit to the published data directly gives a similar consistent result of $\langle p_T \rangle = (0.284 \pm 0.015) [\text{GeV}/c] + (0.506 \pm 0.033)m_0$. For baryons the agreement with the linear fit is reasonable based on the data published by the STAR experiment.

In the original work of R. Hagedorn [22] a nearly linear dependence of the $\langle p_T \rangle$ was derived based on the assumption of Boltzmann-Gibbs statistics to describe the particle spectra at low p_T . The difference between mesons and baryons would follow from the bosonic and fermionic nature of these particles. However, quantitatively the values of the particle $\langle p_T \rangle$ and the magnitude of the meson-to-baryon difference are not the same as would follow from the mechanisms discussed in [22].

The lower panel of Fig. 17 shows the ratio of the integrated yields published by the experiment to the integrated yields extracted from the Tsallis function fits. The common uncertainties on all integrated yields of 9.7% for PHENIX and 12% for STAR are not included. Most of the ratios equal 1 within uncertainties. From Fig. 17 and Table IX one may conclude that the constrained Tsallis fit reproduces the measured integrated cross section with

high accuracy for all identified particles in $p + p$ collisions at $\sqrt{s} = 200$ GeV. This gives justification to use the constrained Tsallis fit results to obtain $d\sigma/dy$ for particles which have only been measured in a limited p_T range, such as π^0 , η , and η' mesons. The resulting $d\sigma/dy$ for such particles are also given in Table IX.

It should be noted explicitly that the $d\sigma/dy$ and $\langle p_T \rangle$ values given in Table IX determined using the Tsallis parametrization do not supersede, or presume to be more accurate than, the corresponding values published by the experiments in the original papers. They are given to validate the method. In those cases where no values have been published, the Tsallis fit result values in the table represent a best attempt to obtain the cross section or $\langle p_T \rangle$ based on the validity of the Tsallis fit distribution.

D. Statistical model calculation

Figure 18 shows the ratio of the constrained Tsallis fit results for the integrated particle yields to the predicted yields from a statistical model (SM) calculation [75]. The data-to-model ratio for PHENIX data is shown in the upper panel, and for STAR data in the lower panel. The statistical model calculation parameters were chosen to reproduce the integrated yields published by the STAR experiment [8–10,63,73,74], which may explain the larger discrepancies in the comparison to the PHENIX results.

Although statistical models are not commonly used to describe $p + p$ data, the agreement of the statistical model calculation with the STAR results was found to be accurate for most particles except for the ρ , ϕ , and Λ^* [40]. Leaving

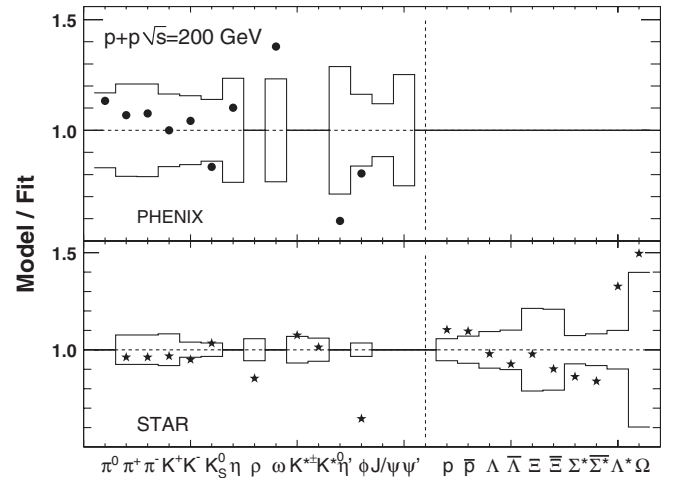


FIG. 18. Ratio of integrated yields predicted by the statistical model [40] to those of the constrained Tsallis fits for various particles. Results for fits to PHENIX data are shown in the upper panel and STAR data in the lower panel. The band reflects the uncertainty of the Tsallis fit results and includes the trigger uncertainty of 9.7% for PHENIX. The lower panel has smaller uncertainties because the model prediction was based on published STAR data given in Table IX. There are no points outside the plot boundaries. The vertical dashed line separates mesons and baryons.

aside baryons, for which the calculations of the $d\sigma/dy$ requires additional assumptions, as explained above, the Tsallis fit also has difficulty reproducing the result for the ρ meson, as shown in Fig. 17. This can be explained by the large systematic uncertainty of the published value [73].

For the PHENIX data the SM calculations agree with the production rates for most mesons because the Tsallis fit results of the PHENIX and STAR data agree. The production rates of π^0 , η , ω , η' , and ϕ were not measured by STAR and so were not used in the determination of the SM parameters. Among them, the predicted yields of π^0 and η mesons are in very good agreement with the PHENIX data. The predictions of the SM for the ω , η' , and ϕ yields are less accurate, with ratios just outside of errors.

VI. SUMMARY

A systematic study of neutral meson production in $p + p$ collisions at $\sqrt{s} = 200$ GeV has been performed by the PHENIX experiment at RHIC with results presented in this paper. New measurements by PHENIX of K_S^0 , ω , ϕ , and η' meson production have been presented.

The measurement of the K_S^0 invariant differential cross section via the $\pi^0\pi^0$ decay channel in the momentum range $2 < p_T$ (GeV/c) < 13.5 extends previously published K^\pm measurements [1].

We present the first measurement of the ϕ invariant differential cross section in the K^+K^- decay mode using several different techniques. The combined spectrum reaches to $p_T = 8$ GeV/c.

This work also presents the first measurement of the invariant differential cross section of η' production measured via the $\eta\pi^+\pi^-$ decay mode with results that cover the range $3 < p_T$ (GeV/c) < 11 .

Measurements of ω meson production in nonleptonic decay channels extend the p_T coverage of the previous PHENIX ω measurement [4], obtained with a smaller data sample, to 13.5 GeV/c.

These first measurements of the ω and ϕ in the e^+e^- decay channel extend the p_T coverage for these two particles down to zero momentum and allow a direct calculation of the integrated yields and mean transverse momenta with the following results: $d\sigma^\omega/dy = 4.20 \pm 0.33^{\text{stat}} \pm 0.52^{\text{syst}}$ mb and $d\sigma^\phi/dy = 0.432 \pm 0.031^{\text{stat}} \pm 0.051^{\text{syst}}$ mb, and $\langle p_T^\omega \rangle = 0.664 \pm 0.037^{\text{stat}} \pm 0.012^{\text{syst}}$ GeV/c and $\langle p_T^\phi \rangle = 0.752 \pm 0.032^{\text{stat}} \pm 0.014^{\text{syst}}$ GeV/c.

All measured results were found to be consistent between the different decay modes and analysis techniques, as well as with previously published data. The results are shown in Figs. 11 and 12, and the measured cross sections are tabulated in the Appendix.

The invariant differential cross sections for all measured hadrons produced in $p + p$ collisions at $\sqrt{s} = 200$ GeV presented in this work, as well as in previous PHENIX publications, were shown to be described well over the

entire momentum range by the Tsallis distribution functional form with only two parameters, T and n , characterizing the low- and high- p_T regions, respectively. Furthermore, the values of the two parameters extracted from the fits are approximately the same for all measured mesons with a weak mass dependence: $T = 112.6 \pm 3.8 + (11.8 \pm 7.0)m_0$ [GeV/c²] MeV and $n = 9.48 \pm 0.14 + (0.66 \pm 0.39)m_0$ [GeV/c²].

The meson spectral shapes have very similar forms when plotted as a function of m_T and hence follow m_T scaling well at $\sqrt{s} = 200$ GeV. On the other hand, the proton spectra are described with a significantly lower parameter value of $T = 58.8 \pm 6.4$ MeV and do not follow the m_T -scaling form observed for mesons.

The ability to successfully describe all particle spectra in $p + p$ collisions at $\sqrt{s} = 200$ GeV with a common functional form allows one to calculate the invariant differential cross section for any particle. This allows the absolute integrated yield to be derived from any experimental measurement of the hadron spectrum, even with limited p_T range. The values of $d\sigma/dy$ and $\langle p_T \rangle$ are tabulated in Table IX for hadrons measured by PHENIX, as well as those measured by the STAR experiment using the set of values of Tables V and VII. For all measured mesons the average transverse momentum of the particle depends linearly on the mass m_0 and can be parametrized with the relation $\langle p_T \rangle = (0.319 \pm 0.007)$ [GeV/c] $+ (0.491 \pm 0.009)m_0$.

The predictions of statistical model calculations based on data published by the STAR experiment [40] were shown to be in good agreement with the integrated yields calculated from the Tsallis distribution fits for most particles. Some deviations are seen for the ω , the η' , and the ϕ mesons.

ACKNOWLEDGMENTS

We thank the staff of the Collider-Accelerator and Physics Departments at Brookhaven National Laboratory and the staff of the other PHENIX participating institutions for their vital contributions. We also thank F. Becattini of the University of Florence for providing us with the statistical model predictions, and G. Wilk of SINS, Warsaw for useful discussions about applications of the Tsallis distribution. We acknowledge support from the Office of Nuclear Physics in the Office of Science of the Department of Energy, the National Science Foundation, a sponsored research grant from Renaissance Technologies LLC, Abilene Christian University Research Council, Research Foundation of SUNY, and Dean of the College of Arts and Sciences, Vanderbilt University (U.S.); Ministry of Education, Culture, Sports, Science, and Technology and the Japan Society for the Promotion of Science (Japan); Conselho Nacional de Desenvolvimento Científico e Tecnológico and Fundação de Amparo à Pesquisa do Estado de São Paulo (Brazil); Natural Science Foundation of China (People's Republic of China); Ministry of Education, Youth and Sports (Czech Republic); Centre National de la

Recherche Scientifique, Commissariat à l'Énergie Atomique, and Institut National de Physique Nucléaire et de Physique des Particules (France); Ministry of Industry, Science and Technologies, Bundesministerium für Bildung und Forschung, Deutscher Akademischer Austausch Dienst, and Alexander von Humboldt Stiftung (Germany); Hungarian National Science Fund, OTKA (Hungary); Department of Atomic Energy (India); Israel Science Foundation (Israel); National Research Foundation (Korea); Ministry of Education and Science, Russia Academy of Sciences, Federal Agency of Atomic Energy

(Russia); VR and the Wallenberg Foundation (Sweden); the U.S. Civilian Research and Development Foundation for the Independent States of the Former Soviet Union; the U.S.-Hungarian Fulbright Foundation for Educational Exchange; and the U.S.-Israel Binational Science Foundation.

APPENDIX

Tables X and XI show the measured invariant differential cross section $\frac{1}{2\pi p_T} \frac{d^2\sigma}{dy dp_T}$.

TABLE X. The invariant differential cross section $\frac{1}{2\pi p_T} \frac{d^2\sigma}{dy dp_T}$ of ω meson production measured in the indicated decay channel. Notations are as follows: V is the differential cross section, and A, B, and C are the three types of errors described in the text.

Meson	Decay channel	p_T GeV/ c	V mb/(GeV/ c) ²	A	B	C
ω	e^+e^-	0.125	3.5	1.1	0.4	0.2
		0.375	1.76	0.33	0.19	$8. \times 10^{-2}$
		0.625	1.12	0.12	0.12	$5. \times 10^{-2}$
		0.875	0.425	5.6×10^{-2}	4.6×10^{-2}	1.9×10^{-2}
		1.125	0.213	2.8×10^{-2}	2.3×10^{-2}	$2. \times 10^{-3}$
		1.375	9.0×10^{-2}	1.4×10^{-2}	$1. \times 10^{-2}$	$4. \times 10^{-3}$
		1.75	2.73×10^{-2}	4.6×10^{-3}	2.9×10^{-3}	1.2×10^{-3}
		2.5	3.34×10^{-3}	6.3×10^{-4}	3.5×10^{-4}	1.5×10^{-4}
		3.5	3.6×10^{-4}	1.2×10^{-4}	$4. \times 10^{-5}$	$2. \times 10^{-5}$
		2.25	8.0×10^{-3}	1.4×10^{-3}	$8. \times 10^{-4}$	2.6×10^{-4}
		2.75	2.50×10^{-3}	2.5×10^{-4}	2.4×10^{-4}	$8. \times 10^{-5}$
		3.25	7.89×10^{-4}	5.8×10^{-5}	7.4×10^{-5}	2.6×10^{-5}
		3.75	2.56×10^{-4}	1.7×10^{-5}	2.3×10^{-5}	$8. \times 10^{-6}$
		4.25	9.41×10^{-5}	5.9×10^{-6}	8.0×10^{-6}	3.1×10^{-6}
		4.75	3.69×10^{-5}	2.5×10^{-6}	3.5×10^{-6}	1.2×10^{-6}
		5.25	1.68×10^{-5}	1.3×10^{-6}	1.5×10^{-6}	$5. \times 10^{-7}$
ω	$\pi^0\pi^+\pi^-$	5.75	7.57×10^{-6}	7.1×10^{-7}	7.1×10^{-7}	2.5×10^{-7}
		6.25	3.89×10^{-6}	4.1×10^{-7}	3.7×10^{-7}	1.3×10^{-7}
		6.75	2.13×10^{-6}	2.8×10^{-7}	2.2×10^{-7}	$7. \times 10^{-8}$
		7.25	1.45×10^{-6}	2.2×10^{-7}	1.6×10^{-7}	$5. \times 10^{-8}$
		7.75	8.5×10^{-7}	1.6×10^{-7}	1.0×10^{-7}	$3. \times 10^{-8}$
		8.25	4.03×10^{-7}	9.8×10^{-8}	4.6×10^{-8}	1.3×10^{-8}
		8.75	2.93×10^{-7}	7.0×10^{-8}	3.6×10^{-8}	1.0×10^{-8}
		9.25	2.48×10^{-7}	6.2×10^{-8}	3.5×10^{-8}	$8. \times 10^{-9}$
		9.75	1.49×10^{-7}	4.0×10^{-8}	2.2×10^{-8}	$5. \times 10^{-9}$
		10.25	1.09×10^{-7}	3.0×10^{-8}	1.7×10^{-8}	$4. \times 10^{-9}$
		10.75	6.0×10^{-8}	1.9×10^{-8}	$1. \times 10^{-8}$	$2. \times 10^{-9}$
		11.25	5.1×10^{-8}	1.6×10^{-8}	$8. \times 10^{-9}$	$2. \times 10^{-9}$
ω	$\pi^0\gamma$	12.	2.41×10^{-8}	8.3×10^{-9}	3.6×10^{-9}	$8. \times 10^{-10}$
		13.	1.02×10^{-8}	4.4×10^{-9}	1.7×10^{-9}	$3. \times 10^{-10}$
		2.5	4.15×10^{-3}	5.0×10^{-4}	5.5×10^{-4}	2.3×10^{-4}
		3.5	4.54×10^{-4}	3.2×10^{-5}	4.9×10^{-5}	2.5×10^{-5}
		4.5	5.07×10^{-5}	4.8×10^{-6}	5.2×10^{-6}	2.8×10^{-6}
		5.5	1.14×10^{-5}	1.8×10^{-6}	1.1×10^{-6}	$6. \times 10^{-7}$
		6.5	3.33×10^{-6}	4.5×10^{-7}	3.8×10^{-7}	1.8×10^{-7}
		7.5	7.7×10^{-7}	2.0×10^{-7}	1.0×10^{-7}	$4. \times 10^{-8}$
		9.	1.94×10^{-7}	6.4×10^{-8}	2.9×10^{-8}	1.1×10^{-8}
		11.	4.8×10^{-8}	1.6×10^{-8}	1.0×10^{-8}	$3. \times 10^{-9}$

TABLE XI. The invariant differential cross section $\frac{1}{2\pi p_T} \frac{d^2\sigma}{dy dp_T}$ of K_S^0 , η' , and ϕ meson production measured in the indicated decay channel. Notations are as follows: V is the differential cross section, and A, B, and C are the three types of errors described in the text.

Meson	Decay channel	p_T GeV/ c	V mb/(GeV/ c) ²	A	B	C
K_S^0	$\pi^0 \pi^0$	2.25	4.66×10^{-3}	7.7×10^{-4}	7.4×10^{-4}	3.0×10^{-4}
		2.75	1.30×10^{-3}	1.1×10^{-4}	1.8×10^{-4}	8.0×10^{-5}
		3.25	4.14×10^{-4}	2.5×10^{-5}	5.5×10^{-5}	2.6×10^{-5}
		3.75	1.54×10^{-4}	8.0×10^{-6}	2.0×10^{-5}	1.0×10^{-5}
		4.25	5.09×10^{-5}	2.8×10^{-6}	6.6×10^{-6}	3.2×10^{-6}
		4.75	2.22×10^{-5}	1.2×10^{-6}	2.9×10^{-6}	1.4×10^{-6}
		5.25	1.06×10^{-5}	6.0×10^{-7}	1.4×10^{-6}	7.0×10^{-7}
		5.75	4.74×10^{-6}	3.3×10^{-7}	6.1×10^{-7}	3.0×10^{-7}
		6.25	2.74×10^{-6}	2.2×10^{-7}	3.6×10^{-7}	1.7×10^{-7}
		6.75	1.30×10^{-6}	1.3×10^{-7}	1.7×10^{-7}	8.0×10^{-8}
		7.25	7.70×10^{-7}	1.0×10^{-7}	1.0×10^{-7}	5.0×10^{-8}
		7.75	3.82×10^{-7}	6.0×10^{-8}	5.3×10^{-8}	2.4×10^{-8}
		8.25	2.88×10^{-7}	4.4×10^{-8}	4.1×10^{-8}	1.8×10^{-8}
		8.75	1.59×10^{-7}	3.1×10^{-8}	2.3×10^{-8}	1.0×10^{-8}
		9.50	7.80×10^{-8}	1.2×10^{-8}	1.1×10^{-8}	4.9×10^{-9}
		10.5	3.49×10^{-8}	8.5×10^{-9}	5.6×10^{-9}	2.2×10^{-9}
		11.5	1.25×10^{-8}	3.7×10^{-9}	2.2×10^{-9}	8.0×10^{-10}
		12.75	6.50×10^{-9}	2.1×10^{-9}	1.3×10^{-9}	4.1×10^{-10}
η'	$\eta \pi^+ \pi^-$	3.25	1.53×10^{-4}	3.6×10^{-5}	1.6×10^{-5}	$7. \times 10^{-6}$
		3.75	7.38×10^{-5}	8.9×10^{-6}	7.3×10^{-6}	3.3×10^{-6}
		4.25	2.55×10^{-5}	4.1×10^{-6}	2.5×10^{-6}	1.1×10^{-6}
		4.75	1.39×10^{-5}	2.0×10^{-6}	1.3×10^{-6}	$6. \times 10^{-7}$
		5.25	4.9×10^{-6}	1.0×10^{-6}	$5. \times 10^{-7}$	$2. \times 10^{-7}$
		5.75	2.32×10^{-6}	4.3×10^{-7}	2.3×10^{-7}	1.0×10^{-7}
		6.25	1.13×10^{-6}	3.1×10^{-7}	1.1×10^{-7}	$5. \times 10^{-8}$
		6.75	7.7×10^{-7}	1.7×10^{-7}	$8. \times 10^{-8}$	$3. \times 10^{-8}$
		7.5	2.33×10^{-7}	5.4×10^{-8}	2.7×10^{-8}	1.0×10^{-8}
		8.5	1.07×10^{-7}	3.3×10^{-8}	1.2×10^{-8}	$5. \times 10^{-9}$
		9.5	5.2×10^{-8}	1.7×10^{-8}	$6. \times 10^{-9}$	$2. \times 10^{-9}$
		10.75	1.09×10^{-8}	5.8×10^{-9}	2.1×10^{-9}	4.9×10^{-10}
ϕ	$e^+ e^-$	0.125	0.264	6.3×10^{-2}	2.6×10^{-2}	1.1×10^{-2}
		0.375	0.188	3.1×10^{-2}	1.8×10^{-2}	$8. \times 10^{-3}$
		0.625	8.9×10^{-2}	1.5×10^{-2}	$9. \times 10^{-3}$	$4. \times 10^{-3}$
		0.875	5.83×10^{-2}	8.2×10^{-3}	5.8×10^{-3}	2.5×10^{-3}
		1.125	2.57×10^{-2}	4.3×10^{-3}	2.5×10^{-3}	1.2×10^{-3}
		1.375	1.31×10^{-2}	2.7×10^{-3}	1.3×10^{-3}	$6. \times 10^{-4}$
		1.75	2.79×10^{-3}	7.5×10^{-4}	2.8×10^{-4}	1.3×10^{-4}
		2.5	7.2×10^{-4}	1.5×10^{-4}	$7. \times 10^{-5}$	$3. \times 10^{-5}$
		3.5	9.7×10^{-5}	3.1×10^{-5}	1.0×10^{-5}	$4. \times 10^{-6}$
		1.1	3.32×10^{-2}	2.6×10^{-3}	2.6×10^{-3}	$4. \times 10^{-4}$
ϕ	$K^+ K^-$	1.45	1.01×10^{-2}	$7. \times 10^{-4}$	$5. \times 10^{-4}$	$1. \times 10^{-4}$
		1.95	3.16×10^{-3}	1.9×10^{-4}	1.7×10^{-4}	$4. \times 10^{-5}$
		2.45	9.28×10^{-4}	5.6×10^{-5}	5.3×10^{-5}	1.1×10^{-5}
		2.95	2.99×10^{-4}	1.9×10^{-5}	1.8×10^{-5}	$4. \times 10^{-6}$
		3.45	1.02×10^{-4}	$6. \times 10^{-6}$	$6. \times 10^{-6}$	$1. \times 10^{-6}$
		3.95	3.49×10^{-5}	2.6×10^{-6}	2.3×10^{-6}	$4. \times 10^{-7}$
		4.45	1.38×10^{-5}	1.8×10^{-6}	$9. \times 10^{-7}$	$2. \times 10^{-7}$
		5.5	2.31×10^{-6}	4.1×10^{-7}	1.6×10^{-7}	$3. \times 10^{-8}$
		7.	3.21×10^{-7}	7.9×10^{-8}	2.4×10^{-8}	$4. \times 10^{-9}$

- [1] S. S. Adler *et al.* (PHENIX Collaboration), *Phys. Rev. C* **74**, 024904 (2006).
- [2] S. S. Adler *et al.* (PHENIX Collaboration), *Phys. Rev. C* **75**, 024909 (2007).
- [3] A. Adare *et al.* (PHENIX Collaboration), *Phys. Rev. D* **76**, 051106 (2007).
- [4] S. S. Adler *et al.* (PHENIX Collaboration), *Phys. Rev. C* **75**, 051902 (2007).
- [5] A. Adare *et al.* (PHENIX Collaboration), *Phys. Rev. Lett.* **98**, 232002 (2007).
- [6] A. Adare *et al.* (PHENIX Collaboration), *Phys. Rev. D* **83**, 032001 (2011).
- [7] J. Adams *et al.* (STAR Collaboration), *Phys. Lett. B* **637**, 161 (2006).
- [8] B. Abelev *et al.* (STAR Collaboration), *Phys. Rev. C* **79**, 034909 (2009).
- [9] B. Abelev *et al.* (STAR Collaboration), *Phys. Rev. C* **75**, 064901 (2007).
- [10] B. Abelev *et al.* (STAR Collaboration), *Phys. Rev. Lett.* **97**, 132301 (2006).
- [11] J. Adams *et al.* (STAR Collaboration), *Phys. Lett. B* **616**, 8 (2005).
- [12] D. Antreasyan *et al.*, *Phys. Rev. D* **19**, 764 (1979).
- [13] D. E. Jaffe *et al.* (FNAL-E605 Collaboration), *Phys. Rev. D* **40**, 2777 (1989).
- [14] B. Alper *et al.* (British-Scandinavian Collaboration), *Nucl. Phys.* **B100**, 237 (1975).
- [15] F. W. Busser *et al.*, *Nucl. Phys.* **B106**, 1 (1976).
- [16] M. G. Albrow *et al.* (CHLM Collaboration), *Nucl. Phys.* **B56**, 333 (1973).
- [17] K. Guettler *et al.* (British-Scandinavian-MIT Collaboration), *Nucl. Phys.* **B116**, 77 (1976).
- [18] K. Guettler *et al.* (British-Scandinavian-MIT Collaboration), *Phys. Lett.* **64B**, 111 (1976).
- [19] D. E. Acosta *et al.* (CDF Collaboration), *Phys. Rev. D* **72**, 052001 (2005).
- [20] G. Sterman *et al.*, *Rev. Mod. Phys.* **67**, 157 (1995).
- [21] R. Hagedorn, *Nuovo Cimento Suppl.* **3**, 147 (1965).
- [22] R. Hagedorn, *Riv. Nuovo Cimento Soc. Ital. Fis.* **6N10**, 1 (1984).
- [23] J. Bartke *et al.* (Aachen-Berlin-Bonn-CERN-Cracow-Heidelberg-Warsaw Collaboration), *Nucl. Phys.* **B120**, 14 (1977).
- [24] C. Tsallis, *J. Stat. Phys.* **52**, 479 (1988).
- [25] G. Wilk and Z. Wlodarczyk, *Phys. Rev. Lett.* **84**, 2770 (2000).
- [26] M. Biyajima, M. Kaneyama, T. Mizoguchi, and G. Wilk, *Eur. Phys. J. C* **40**, 243 (2005).
- [27] M. Biyajima *et al.*, *Eur. Phys. J. C* **48**, 597 (2006).
- [28] Z. Tang *et al.*, *Phys. Rev. C* **79**, 051901 (2009).
- [29] M. Shao *et al.*, *J. Phys. G* **37**, 085104 (2010).
- [30] V. Khachatryan *et al.* (CMS Collaboration), *J. High Energy Phys.* **02** (2010) 041.
- [31] M. Nauenberg, *Phys. Rev. E* **67**, 036114 (2003).
- [32] C. Tsallis, *Phys. Rev. E* **69**, 038101 (2004).
- [33] M. Nauenberg, *Phys. Rev. E* **69**, 038102 (2004).
- [34] A. S. Parvan, *Phys. Lett. A* **360**, 26 (2006).
- [35] T. S. Biro and G. Purcsel, [arXiv:0809.4768](https://arxiv.org/abs/0809.4768).
- [36] Q. A. Wang *et al.*, *Europhys. Lett.* **65**, 606 (2004).
- [37] J. Cleymans and H. Satz, *Z. Phys. C* **57**, 135 (1993).
- [38] P. Braun-Munzinger *et al.*, *Phys. Lett. B* **465**, 15 (1999).
- [39] F. Becattini and U. W. Heinz, *Z. Phys. C* **76**, 269 (1997).
- [40] F. Becattini, P. Castorina, A. Milov, and H. Satz, *Eur. Phys. J. C* **66**, 377 (2010).
- [41] K. Adcox *et al.* (PHENIX Collaboration), *Nucl. Instrum. Methods Phys. Res., Sect. A* **499**, 469 (2003).
- [42] S. Aronson *et al.* (PHENIX Collaboration), *Nucl. Instrum. Methods Phys. Res., Sect. A* **499**, 480 (2003).
- [43] K. Adcox *et al.* (PHENIX Collaboration), *Nucl. Instrum. Methods Phys. Res., Sect. A* **499**, 489 (2003).
- [44] K. Adcox *et al.* (PHENIX Collaboration), *Nucl. Instrum. Methods Phys. Res., Sect. A* **497**, 263 (2003).
- [45] M. Aizawa *et al.* (PHENIX Collaboration), *Nucl. Instrum. Methods Phys. Res., Sect. A* **499**, 508 (2003).
- [46] M. Allen *et al.* (PHENIX Collaboration), *Nucl. Instrum. Methods Phys. Res., Sect. A* **499**, 549 (2003).
- [47] S. S. Adler *et al.* (PHENIX Collaboration), *Phys. Rev. Lett.* **91**, 241803 (2003).
- [48] A. Adare *et al.* (PHENIX Collaboration), *Phys. Rev. D* **82**, 012001 (2010).
- [49] L. Aphecetche *et al.* (PHENIX Collaboration), *Nucl. Instrum. Methods Phys. Res., Sect. A* **499**, 521 (2003).
- [50] C. Amsler *et al.* (PDG Collaboration), *Phys. Lett. B* **667**, 1 (2008 and 2009 partial update for the 2010 edition).
- [51] A. Adare *et al.* (PHENIX Collaboration), [arXiv:1004.3532](https://arxiv.org/abs/1004.3532).
- [52] T. Armstrong *et al.* (FNAL-E760 Collaboration), *Phys. Rev. D* **54**, 7067 (1996).
- [53] A. Spiridonov, [arXiv:hep-ex/0510076](https://arxiv.org/abs/hep-ex/0510076); Internal Note No. DESY-04-105.
- [54] C. Alff *et al.*, *Phys. Rev. Lett.* **9**, 325 (1962).
- [55] J. S. Danburg *et al.*, *Phys. Rev. D* **2**, 2564 (1970).
- [56] S. Giovannella *et al.* (KLOE Collaboration), [arXiv:hep-ex/0505074](https://arxiv.org/abs/hep-ex/0505074).
- [57] M. L. Stevenson *et al.*, *Phys. Rev.* **125**, 687 (1962).
- [58] R. A. Briere *et al.* (CLEO Collaboration), *Phys. Rev. Lett.* **84**, 26 (2000).
- [59] N. Beisert and B. Borasoy, *Nucl. Phys.* **A705**, 433 (2002).
- [60] G. D. Lafferty and T. R. Wyatt, *Nucl. Instrum. Methods Phys. Res., Sect. A* **355**, 541 (1995).
- [61] A. Adare *et al.* (PHENIX Collaboration) (to be published).
- [62] D. de Florian and R. Sassot, *Phys. Rev. D* **69**, 074028 (2004).
- [63] J. Adams *et al.* (STAR Collaboration), *Phys. Rev. C* **71**, 064902 (2005).
- [64] G. Wilk and Z. Wlodarczyk, *Eur. Phys. J. A* **40**, 299 (2009).
- [65] G. Wilk and Z. Wlodarczyk, *Nucl. Phys. B, Proc. Suppl.* **75**, 191 (1999).
- [66] I. Bediaga *et al.*, *Physica A (Amsterdam)* **286**, 156 (2000).
- [67] C. Tsallis, *Physica A (Amsterdam)* **344**, 718 (2004).
- [68] F. Navarra *et al.*, *Physica A (Amsterdam)* **344**, 568 (2004).
- [69] C. Tsallis (updated), <http://tsallis.cat.cbpf.br/biblio.htm>.

- [70] D.B. Walton and J. Rafelski, *Phys. Rev. Lett.* **84**, 31 (2000).
- [71] K. Adcox *et al.* (PHENIX Collaboration), *Phys. Rev. C* **69**, 024904 (2004).
- [72] A. Adare *et al.* (PHENIX Collaboration), *Phys. Rev. C* **77**, 064907 (2008).
- [73] J. Adams *et al.* (STAR Collaboration), *Phys. Rev. Lett.* **92**, 092301 (2004).
- [74] J. Adams *et al.* (STAR Collaboration), *Phys. Lett. B* **612**, 181 (2005).
- [75] F. Becattini and R. Fries, *arXiv:0907.1031*.